ARTICLE IN PRESS

Ocean Engineering xxx (xxxx) xxx

Contents lists available at ScienceDirect

Ocean Engineering

journal homepage: www.elsevier.com/locate/oceaneng

Experimental and numerical comparisons of a dual-flap floating oscillating surge wave energy converter in regular waves

Kelley Ruehl [a,*], Dominic D. Forbush [a], Yi-Hsiang Yu [b], Nathan Tom [b]

[a] Sandia National Laboratories, Albuquerque, NM, United States of America
[b] National Renewable Energy Laboratory, Golden, Colorado, United States of America

ARTICLE INFO

Keywords:
Wave energy
Experimental testing
Numerical simulation
WEC-Sim
Validation

ABSTRACT

The floating oscillating surge wave energy converter (FOSWEC) is a wave energy converter that was designed, built, and tested to develop an open-access data set for the purpose of numerical model validation. This paper details the experimental testing of the 1:33-scale FOSWEC in a directional wave basin, and compares experimental data to numerical simulations using the wave energy converter simulator (WEC-Sim) open-source code. The FOSWEC consists of a floating platform moving in heave, pitch, and surge, and two pitching flaps. Power is extracted through relative motion between each of the flaps and the platform. The device was designed to constrain different degrees of freedom so that it could be configured into a variety of operating conditions with varying dynamics. The FOSWEC was tested in a range of different conditions including: static offset, free decay, forced oscillation, wave excitation, and dynamic response to regular waves. In this paper, results from the range of experimental tests are presented and compared to numerical simulations using the WEC-Sim code.

1. Introduction

Wave energy converters (WECs) are devices designed to generate power by extracting energy from ocean waves. These devices have been conceptualized, researched, and tested for decades. However, most WECs are considered to be at low- to mid-range technology readiness levels (TRLs), and have yet to reach utility-scale commercialization (Weber, 2012). Unlike the wind industry that has largely converged on the three-bladed horizontal-axis wind turbine, the wave energy industry is still evaluating a wide range of design archetypes with fundamentally different operating principles. WECs are often categorized into the follow device types: point absorbers, attenuators, oscillating wave surge devices, oscillating water columns, overtopping devices, and pressure differential devices. However, due to the large range of existing design archetypes, researchers often differ on their categorization of WECs (Cruz, 2008; Lopez et al., 2013). This wide range of design archetypes has made numerical modeling and simulation of WECs a challenging research topic because the numerical requirements between WEC designs vary substantially.

Historically, WECs have been modeled using numerical methods developed for naval architecture, offshore oil and gas applications, or custom-built models for specific devices. More recently, commercial and open-source codes have been developed specifically for modeling WECs. Numerical models of WECs must resolve complex hydrodynamics associated with wave-device interaction, body-to-body interactions, moorings, and electro-mechanical dynamics at the power take-off (PTO) to predict device performance and response. A common numerical approach for simulating WECs is to use the time domain Cummins' impulse response formulation (Cummins, 1962). The Cummins' formulation requires hydrodynamic coefficients for added mass, radiation damping, and wave excitation, details of which are provided in the following section. Using this formulation, the radiation and excitation forces are converted from the frequency domain into their time domain equivalents in the form of impulse response functions through an inverse Fourier transform. Typically, these hydrodynamic coefficients are determined from a frequency domain boundary element method (BEM) solution based on linear potential flow theory. Linear potential flow assumes inviscid fluid, irrotational flow, and small amplitude motion. While this approach is common practice, WEC dynamics in real ocean waves violate these assumptions. The advantage of the Cummins' formulation is that by moving from the frequency domain to the time domain, nonlinearities can be included. This allows for the inclusion of nonlinear effects, such as drag proportional to velocity squared, realistic implementation of nonlinear PTO and control, and modeling of complex mooring systems. The example applications of this numerical approach are numerous, ranging from modeling the SEAREV

* Corresponding author.
E-mail addresses: Kelley.Ruehl@sandia.gov (K. Ruehl), Dominic.Forbush@sandia.gov (D.D. Forbush), Yi-Hsiang.Yu@nrel.gov (Y.-H. Yu), Nathan.Tom@nrel.gov (N. Tom).

https://doi.org/10.1016/j.oceaneng.2019.106575
Received 16 May 2018; Received in revised form 9 August 2019; Accepted 13 October 2019
0029-8018/© 2019 Published by Elsevier Ltd.

Pursuant to the DOE Public Access Plan, this document represents the authors' peer-reviewed, accepted manuscript. The published version of the article is available from the relevant publisher.

Please cite this article as: Kelley Ruehl, *Ocean Engineering*, https://doi.org/10.1016/j.oceaneng.2019.106575

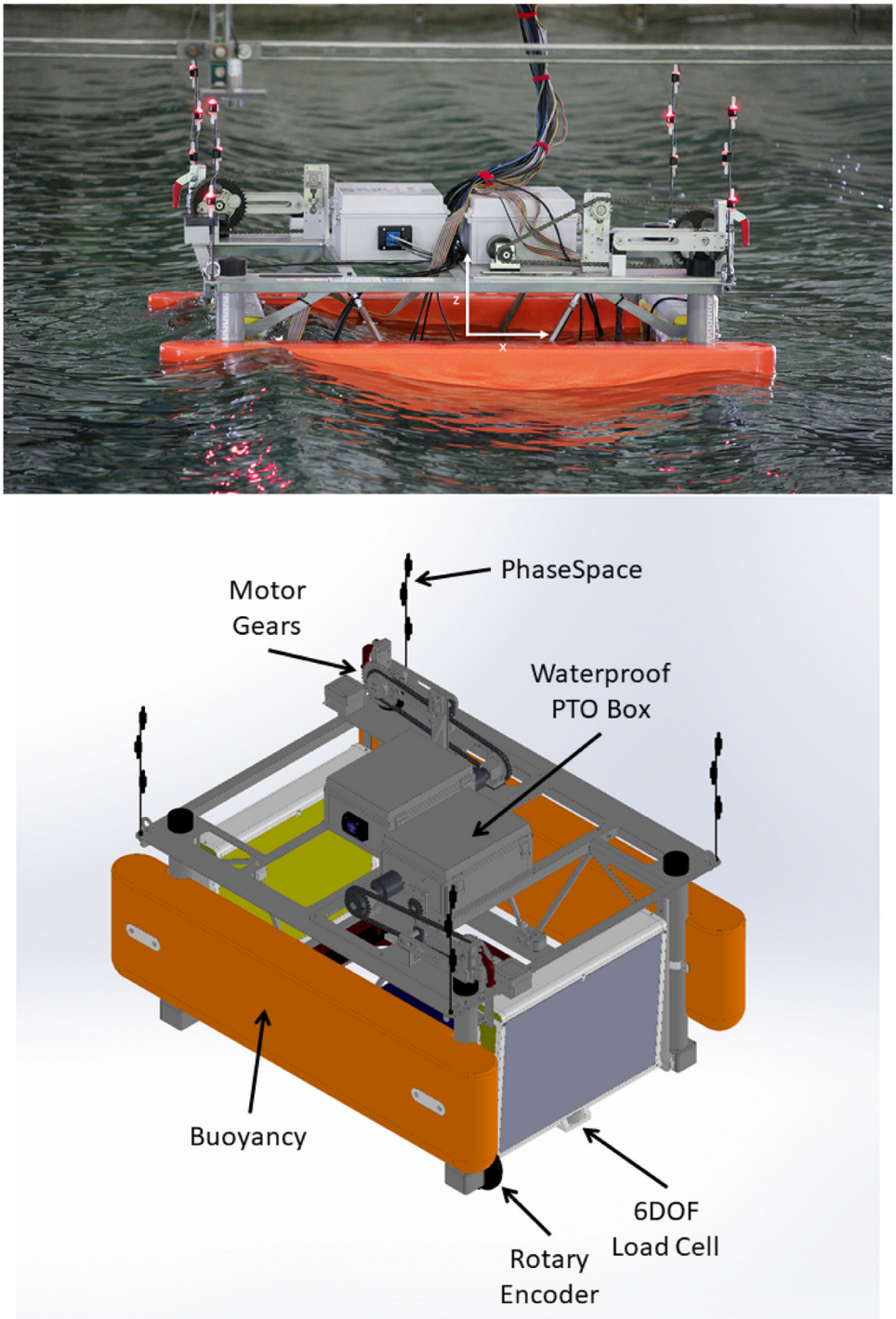

Fig. 1. A 1:33-scale FOSWEC (top) in action during experimental testing with origin at still water line and (bottom) mechanical design rendering with instrumentation. (For interpretation of the references to color in this figure legend, the reader is referred to the web version of this article.)

device, to the Center for Ocean Energy Research modeling competition, to WaveBob- and Powerbuoy-inspired point absorbers, to name a few (Josset et al., 2007; Garcia-Rosa et al., 2015; Beatty et al., 2015). It is worth nothing that while the Cummins' formulation is a common numerical approach, there are many other relevant approaches for modeling WECs. For a detailed review of these methods, refer to Folley (2016).

Model verification and validation are essential for numerical method development, which is commonly used to evaluate the confidence and accuracy of the model. Often, in lieu of validation through comparison to experimental data, numerical models go through verification via comparison to other numerical models (i.e., a code-to-code comparison (Combourieu et al., 2015; Wendt et al., 2017)). On the other hand, to ensure the numerical model accurately represents the physical system, a validation study is often carried out by comparing the numerical solutions to measurements from experimental tests. Due to the wide variations in device archetypes, differences in the dominant physics and intended application, it is preferable to validate these models against WEC-specific experimental data (Lawson et al., 2015; Ruehl et al., 2014). However, the wave energy industry is still in the early stages of development, and developers want to maintain a competitive advantage and preserve their intellectual property. This

Pursuant to the DOE Public Access Plan, this document represents the authors' peer-reviewed, accepted manuscript. The published version of the article is available from the relevant publisher.

Table 1
FOSWEC 1:33-scale mass properties.

Property	Flap 1	Flap 2	Platform
Mass (kg)	23.14	23.19	176.04
X_{cg} (m)	−0.65	0.65	0.0
Y_{cg} (m)	0.0	0.0	0.0
Z_{cg} (m)	−0.29	−0.29	−0.063
I_{xx} (kg m^2)	1.42	1.58	37.88
I_{yy} (kg m^2)	1.19	1.62	29.63
I_{zz} (kg m^2)	1.99	1.25	53.61

means many experimental data sets are not made public, and availability of nonproprietary, open-access data sets for validation is limited. In the last few years, this paradigm has begun to shift, and there is now more focus on development open-access data sets and open-source codes. For example, the U.S. Department of Energy (DOE) now requires data from all projects funded by the Water Power Technologies Office (WPTO) to be posted to the Marine and Hydrokinetic Data Repository (MHKDR) (MHKDR, 2019). In addition to data available from DOE WPTO, similar efforts to share and disseminate data are being made domestically and internationally (OPERA, 2019).

In this study, experimental wave tank tests and numerical simulations of a 1:33-scale floating oscillating surge wave energy converter (FOSWEC) are compared. The FOSWEC was tested in a range of different conditions including: static offset, free decay, forced oscillation, wave excitation, and dynamic response to regular waves in four different device configurations. The numerical simulations are performed using the open-source WEC-Sim code, and the simulation performance is evaluated in an *a priori* sense (i.e., unadvised by experimental data) and *a posteriori*, in which the simulation has been tuned based upon experimental cases. The FOSWEC experimental data is available open-access on the MHKDR, and FOSWEC data processing scripts are available on a public GitHub repository (Sandia National Laboratories, 2019a,b).

2. FOSWEC

The device tested in this validation study is the 1:33-scale FOSWEC, shown in Fig. 1. The FOSWEC consists of a floating platform (orange) with two pitching flaps (yellow). Each flap hinges about a horizontal shaft and generates power through the relative pitch motion between the flap and platform. The flaps each have a PTO system consisting of a gearbox, electric motor, and torque transducer housed in a waterproof PTO box. They are also instrumented with a 6-degree of freedom (DOF) load cell at the connection of the flap to the shaft, and a rotary encoder. A rendering of the FOSWEC with the sensors labeled is shown in Fig. 1.

The x-axis is defined along the incident wave direction at the still water line (SWL), as labeled at the top of Fig. 1. The geometric and mass properties of the FOSWEC were determined from dry tests and are summarized in Table 1 and Fig. 2. All moments of inertia are relative to the center of gravity, c_g. For details on how these tests were performed, refer to Bosma et al. (2016) and Sandia National Laboratories (2019a).

A motion constraint system was designed and built to selectively restrict the FOSWEC's motion, in order to vary the FOSWEC's configuration to isolate individual degrees of freedom. A rendering of the motion constraint arm is shown in Fig. 3. For more information about its design refer to Sandia National Laboratories (2019a). The base of the constraint system is affixed rigidly to the basin floor, and acts as a mooring system for the device. In this way, coupling between modes of motion could be isolated to allow for independent characterization. The available DOF for each of the four configurations is listed in Table 2. For example, in Config 3, both flaps are free to move in pitch, and the platform is allowed to move in heave (implying that the pitch and surge constraints are engaged). A load cell and position sensors were installed on the arm to measure 6-DOF loads and motion in heave, pitch, and surge.

Table 2
Available degrees of freedom by test configuration.

Configuration	Flap in pitch	Platform
Config1	Front flap only	None
Config2	Both flaps	None
Config3	Both flaps	Heave only
Config4	Both flaps	Surge, heave, pitch

Table 3
Motion constraint mass properties.

Property	Heave constraint	Pitch constraint	Surge constraint
Mass (kg)	27.35	4.47	23.66
X_{cg} (m)	0	0	0
Y_{cg} (m)	0	0	0
Z_{cg} (m)	−0.782	−0.366	−0.366
I_{xx} (kg m^2)	2.2	0.29	1.44
I_{yy} (kg m^2)	2.15	0.02	2.21
I_{zz} (kg m^2)	0.28	0.30	3.58

The motion constraint consists of three components: (1) a surge guiderail constraint, (2) pitch constraint, and (3) heave constraint fixed to the basin floor. The mass and inertia properties for the moving components of the motion constraint are defined in Table 3. The mass and inertia of each moving component need to be included in numerical simulations, depending on the motion constraint configuration, details of which will be provided in the following section.

3. WEC-Sim

WEC-Sim is an open-source code developed in MATLAB/Simulink as a library and accompanying scripts that utilize Simscape Multibody to solve for a WEC's rigid body dynamics in the time domain. The code allows users to model complex WEC designs consisting of multiple bodies, PTO systems, mooring systems, and controls for a variety of wave conditions (WEC-Sim, 2019).

WEC-Sim is based on linear wave theory, in which the waves are assumed to be a linear superposition of incident, radiated, and diffracted wave components with added external forcing terms (e.g., PTO and mooring forces) and empirical viscous damping terms. WEC-Sim solves the following time domain equation of motion due to wave forcing for each rigid body around its center of gravity:

$$(m+A_\infty)\ddot{X} = F_{exc}(t) - F_{rad}(t) - F_{hs}(t) - F_{vis}(t) + F_{pto}(t) + F_m(t) + F_{ext}(t) \quad (1)$$

where m is the mass and inertia matrix, A_∞ is the added mass matrix at infinite wave frequency, X is the body's displacement in 6 DOF, and a dot implies a time derivative. $F_{exc}(t)$ is the wave excitation force vector and $F_{rad}(t)$ is the radiation damping force vector, defined as:

$$F_{rad}(t) = \int_0^t k_r(t-\tau)\dot{X}(\tau)d\tau \quad (2)$$

calculated by convolving the radiation impulse response function, k_r, in each DOF, with the 6-element velocity vector, $\dot{X}$. The radiation impulse response function, k_r, is the inverse Fourier transform of radiation damping, defined as:

$$k_r(t) = \frac{2}{\pi}\int_0^\infty B(\omega)\cos(\omega t)d\omega \quad (3)$$

where $B(\omega)$ is radiation damping and ω is wave frequency in rad/s. The hydrostatic restoring force, $F_{hs}(t)$, is defined as:

$$F_{hs}(t) = K_{hs}X \quad (4)$$

where K_{hs} is a 6-by-6 matrix of constant hydrostatic stiffness coefficients with units of N/m in translation and Nm/rad in rotation, and X is a 6-element displacement vector. The viscous force, $F_{vis}(t)$, is defined as:

Pursuant to the DOE Public Access Plan, this document represents the authors' peer-reviewed, accepted manuscript. The published version of the article is available from the relevant publisher.

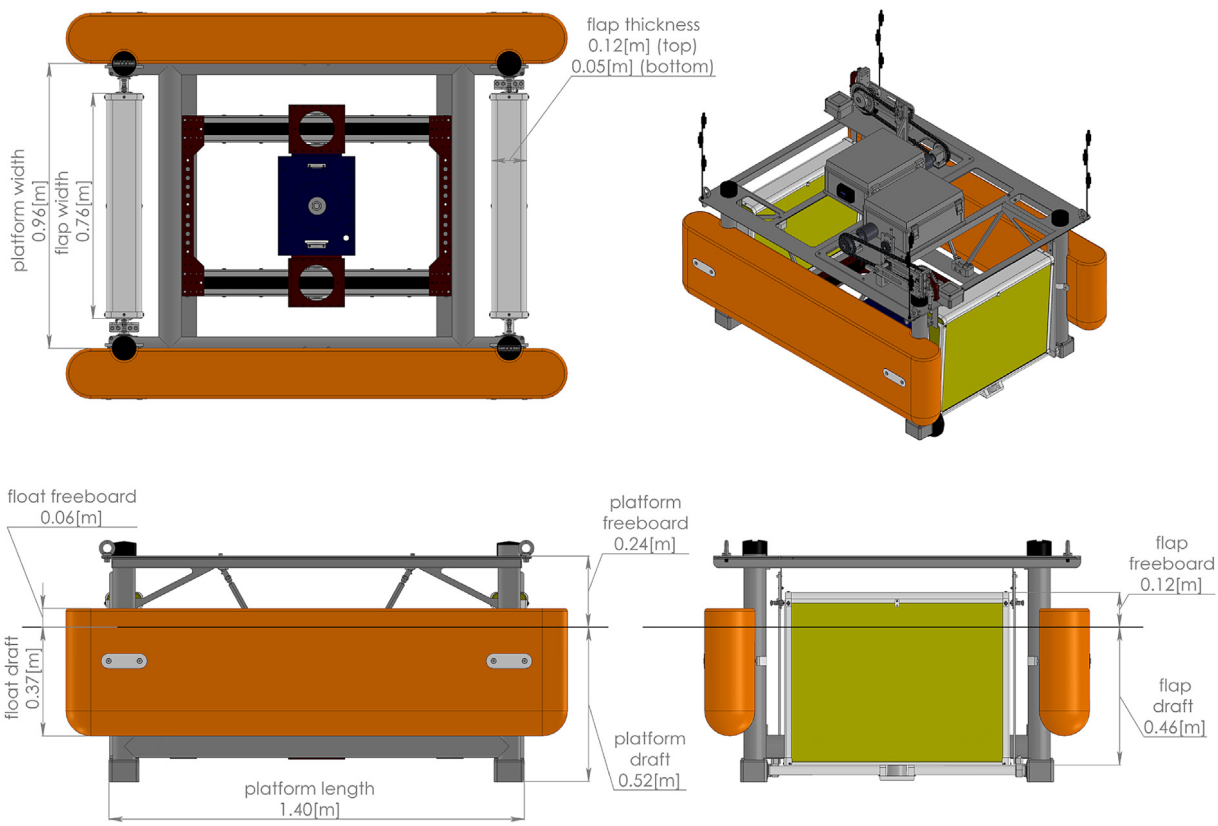

Fig. 2. FOSWEC mechanical design dimensions.

$$F_{vis}(t) = C_v\dot{X} + \frac{C_d \rho A_s}{2}|\dot{X}|\dot{X}$$
$$= C_v\dot{X} + C_D|\dot{X}|\dot{X} \quad (5)$$

where C_v is the linear viscous damping coefficient, and the quadratic drag, C_D, is a function of the drag coefficient, C_d, water density, ρ, and the cross sectional area, A_s. $F_{pto}(t)$ is the force applied on the WEC from the PTO, $F_m(t)$ is the mooring force, and $F_{ext}(t)$ is the external force from joints at the interface between component bodies. The latter force is calculated by the multi-body dynamics solver within Simulink based upon user-defined device geometry, joint parameters, and relative body motions. Further description of each of these forces will be provided in the following sections.

WEC-Sim utilizes hydrodynamic coefficients in the frequency domain, and determines their time domain equivalent in the form of excitation and radiation impulse response functions, and infinite frequency added mass using the Cummins' formulation. These hydrodynamic coefficients are typically determined from BEM solutions, but can also be determined experimentally. For the WEC-Sim solutions presented in this study, the hydrodynamic coefficients were solved for using the BEM code WAMIT (Lee and Newman, 2017). Two WAMIT solutions for the FOSWEC were run with 458 evenly-spaced frequencies from 0.05 to 22.8 rad/s, one for all three bodies, and another for the flap only. The flap only WAMIT solution was run with the origin at the hinge location so that its results could be used for direct comparison to the experimentally determined wave excitation, radiation damping, and added mass. The three-body WAMIT solution was run so solve for body-to-body interactions, and was used for all of the WEC-Sim simulations (e.g., free decay and wave cases). The WAMIT solutions exclude the presence of the motion constraint, which was assumed to have minimal effect on the hydrodynamic parameters of the FOSWEC itself.

The FOSWEC device was simulated in WEC-Sim using the measured mass and inertia properties defined in Tables 1 and 3, and using the hydrodynamic parameters determined from WAMIT, in addition to experimentally determined parameters. Because the determination of some device parameters required limiting available DOF, constrained WEC-Sim models were used in the simulations to be representative of experimental conditions, denoted as Config 1–Config 4. All WEC-Sim simulations were run using the parameters listed in Table 4. An image of the WEC-Sim Simulink model is shown in Fig. 4. The platform (gray) and flaps (yellow) are modeled as hydrodynamic bodies, the motion

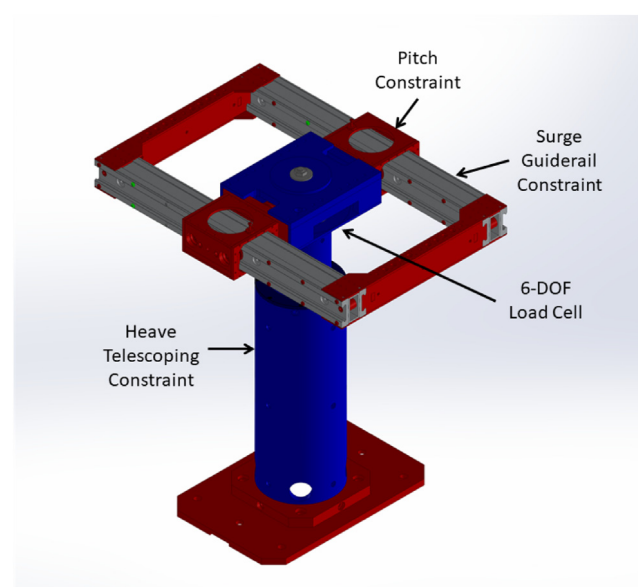

Fig. 3. Rendering of motion constraint.

Pursuant to the DOE Public Access Plan, this document represents the authors' peer-reviewed, accepted manuscript.
The published version of the article is available from the relevant publisher.

Table 4
WEC-Sim simulation parameters.

Description	Value
Wave height (m)	H
Wave period (s)	T
Simulink solver	ode45
Maximum time step (s)	T/200
Wave ramp time (s)	5T
Convolution integral time (s)	25
Simulation end time (s)	20T

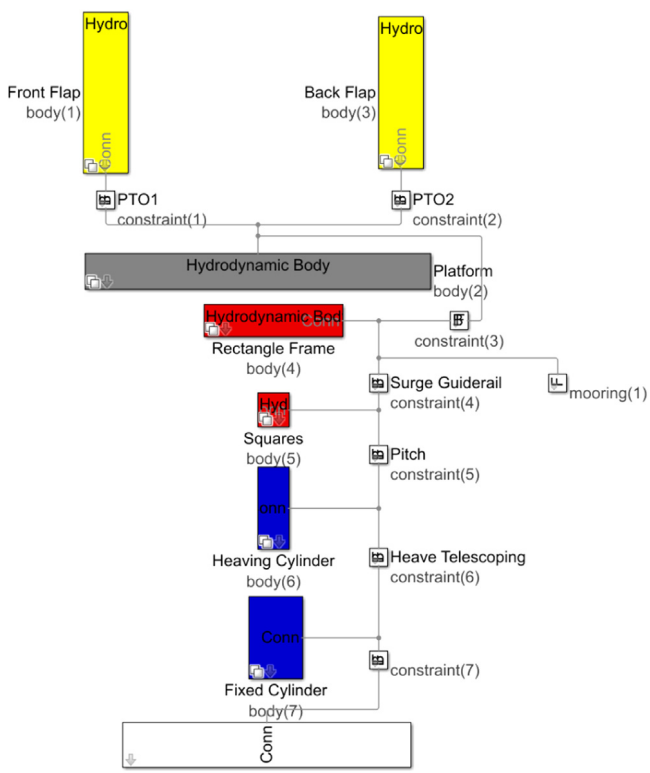

Fig. 4. WEC-Sim model of the FOSWEC and motion constraint implementation in Simulink. (For interpretation of the references to color in this figure legend, the reader is referred to the web version of this article.)

constraint is modeled as four nonhydrodynamic bodies (red and blue), and each of the joints are modeled as constraints (white). Details of the validation effort are described in the following sections.

4. Experiments

The FOSWEC was evaluated in a series of experimental wave tank tests for comparison to the frequency domain WAMIT hydrodynamic coefficients and the time domain WEC-Sim simulations with the experimentally observed device response. The experimental tests were performed in the Directional Wave Basin at the Hinsdale Wave Research Laboratory located at Oregon State University (Hinsdale, 2019). The test objectives were to determine the mass/inertia, the hydrodynamic properties of the FOSWEC components as defined in Eq. (1), and the response of the device when subject to incident waves in different configurations (Table 2). A summary of the experimental wave tank tests performed and their corresponding test objectives is provided in Table 5. This section will provide an explanation of the tests performed and the experimental derivation of the terms defined in Eq. (1). For more information about the tests performed and for a more detailed description of the test facility refer to Bosma et al. (2016) and Ruehl et al. (2016). Unless otherwise noted, device data (e.g., loads, positions) were collected at 100 Hz, and wave sensor data was collected at 50 Hz.

Table 5
Summary of experimental test campaign.

Experiment	Objective
Static offset	Hydrostatic restoring stiffness, K_{hs}
Free decay	Natural frequency, ω_n, and total damping, $C_{tot}(\omega_d)$
Wave excitation	Wave excitation force coefficient, $f_{exc}(\omega)$
Forced oscillation	Added mass, $A(\omega)$, total damping, $C_{tot}(\omega)$, and quadratic drag, C_D
Wave response	Response amplitude operator, RAO

4.1. Static offset

The objective of the static offset test is to determine the hydrostatic restoring coefficient, K_{hs}, in each DOF, namely the flap in pitch and the platform in heave, pitch, and surge. During each test, all DOFs, aside from those being evaluated, were locked. The hydrostatic restoring force, F_{hs}, referenced in Eq. (1), is the force exerted on a submerged body by the static fluid. As defined in Eq. (4), X is a six-element displacement vector, and K_{hs} is a 6-by-6 matrix of constant hydrostatic stiffness coefficients with units of N/m in translation and Nm/rad in rotation. For translation in heave, the hydrostatic stiffness coefficient, k_{33}, is defined as:

$$k_{33} = \rho g A_{wp} \tag{6}$$

where ρ is the density of water, g is the acceleration due to gravity, and A_{wp} is the cut water-plane area. For rotation in pitch, the hydrostatic stiffness coefficient k_{55} is defined as:

$$k_{55} = \rho g I_y + \rho g V z_g - m g z_b \tag{7}$$

where I_y is the second moment of area of the cut water-plane area, V is the submerged volume, z_g is the z-coordinate of the center of gravity, m is the body mass, and z_b is the z-coordinate of the center of buoyancy. It should be noted that while both k_{33} and k_{55} are modeled in WEC-Sim as constant linear spring terms, they are in fact nonlinear. For example, for motion in heave, the cut water plane area, A_{wp}, changes, and for motion in pitch the submerged volume, V, is not constant. It is also worth noting that there is no hydrostatic stiffness in surge (i.e., $k_{11} = 0$). To restore the FOSWEC in surge, a series of rubber bungee cords were installed on both sides of the motion constraint perpendicular to the surge guiderail, and attached to the FOSWEC such that they did not interfere with flap motion. This restoring force is described as surge mooring stiffness, k_m. The hydrostatic and mooring stiffness were determined from a series of static offset tests that will be detailed in the following sections.

4.2. Free decay

The free decay test objectives are to determine the natural frequency, ω_n, and estimate the total linear damping, C_{tot}, for each body in its relevant DOF. Free decay estimates of damping are also used to validate the C_D estimate of flap-pitch forced oscillation tests. Free decay tests were performed for the flap in pitch, and the platform in heave, pitch, and surge. During each test, all DOFs, aside from those being evaluated, were locked. Data processing for each of the decay tests was completed in a similar manner; however, for the sake of brevity, only the analysis of the flap's free decay will be described in this section. With noted exceptions, the same methodology was applied to the platform's free decay tests in heave, pitch, and surge. For these free decay tests, the PTO drivetrain was disconnected. Because the PTO was disconnected, it can be assumed that the flap's free decay response is purely a hydrodynamic response with small frictional forces.

Pursuant to the DOE Public Access Plan, this document represents the authors' peer-reviewed, accepted manuscript. The published version of the article is available from the relevant publisher.

The flap was initially displaced with no incident waves to a prescribed angle and released. The flap motion was then recorded until it returned to steady state at its equilibrium position. Under these test conditions, Eq. (1) simplifies to:

$$(I_{yy} + A_{55})\ddot{\theta} = -C_{tot}\dot{\theta} - C_D|\dot{\theta}|\dot{\theta} - k_{55}\theta \tag{8}$$

where I_{yy} is the moment of inertia in pitch, $A_{55}(\omega_d)$ is the added mass in pitch at the damped natural frequency, $C_{tot}(\omega_d) = B_{55}(\omega_d) + C_v(\omega_d)$ is the total damping due to radiation damping and viscous damping at the damped natural frequency, and θ is the flap angular displacement (equivalent to X_5) (Bosma et al., 2016). Flap angular displacement was low-pass filtered with a first order back-to-back finite-impulse-response filter to remove instrument noise without introducing a phase shift. It should be noted that while $B_{55}(\omega)$ and $C_v(\omega)$ are frequency-dependent damping values, because free decay occurs at the damped natural frequency, only the damping values at the damped natural frequency, $B_{55}(\omega_d)$ and $C_v(\omega_d)$, are relevant. Similarly, the total damping, C_{tot} and C_D are generally frequency-dependent, but only the $C_{tot}(\omega_d)$ and $C_D(\omega_d)$ can be determined from free decay tests.

For decay tests, the damping ratio, ζ, can be determined from time domain data following the logarithmic decrement method using the initial adjacent peaks (Inman, 2008). Based on the experimentally derived ζ, linear damping is defined as:

$$C_{lin}(\omega_d) = 2\zeta(I_{yy} + A_{55})\omega_n \tag{9}$$

where ω_n is the natural frequency calculated from the observed damped natural frequency by:

$$\omega_n = \frac{\sqrt{1-\zeta^2}}{\omega_d} \tag{10}$$

For flap pitch decay, in order to validate the quadratic damping coefficient estimations from the forced oscillation experiments, free-decay damping is temporarily assumed to have solely linear components, expressed as C_{lin}. For different initial displacements, the mass-normalized linear and quadratic components of damping can be estimated at ω_d via linear regression, as suggested by Inman (2008):

$$\frac{F_{vis}}{I_{yy} + A_{55}} = \frac{C_{lin}\dot{\theta}}{I_{yy} + A_{55}} = \frac{C_{tot} + 8C_D\omega|\theta|/(3\pi)}{I_{yy} + A_{55}}\dot{\theta} \tag{11}$$

where mass-normalized damping coefficients are then multiplied by $(I_{yy}+A_{55})$, and A_{55} is estimated from forced oscillation tests at a nearby frequency, then compared to C_{tot} and C_D estimates calculated in an analogous way from forced oscillation tests.

Because forced oscillation tests were not performed for the platform in heave, surge, or pitch, C_D cannot be validated for the platform by this methodology. Therefore, it is assumed that $C_{lin} = C_{tot}$, as calculated via Eq. (9) using BEM estimate of added mass and C_D is used as a simulation tuning parameter.

4.3. Wave excitation

The objective of the wave excitation test is to determine the wave excitation force coefficient, $f_{exc}(\omega)$. For this study only excitation torque on the flap in pitch was considered for direct comparison to the BEM solution from WAMIT. In order to isolate the forces on the flap to those exclusively due to wave excitation, the device was locked in all degrees of freedom during the test. As a result, the left-hand side of Eq. (1) goes to zero. Additionally, because the flap and platform are fixed, the radiation force, F_{rad}, hydrostatic force, F_{hs}, viscous force, F_{vis}, PTO force, F_{pto}, F_{ext}, and mooring force, F_m, are also zero. Thus, the forces measured at the flap load cell will be equal to F_{exc} for this set of experiments.

Wave calibration tests were carried out in the wave tank prior to installation of the FOSWEC. A wave gauge was placed at the future location of the FOSWEC to measure the wave surface elevation at the center of the FOSWEC prior to its installation, and to ensure that the desired wave cases were repeatable. This means that the wave field measured at the device location by this wave gauge includes only the undisturbed incident wave elevation. Additionally, the wave basin was instrumented with an array of wave gauges, both subsea and overhead, that provided other spatially and temporally resolved measurements of the wave field. The parameter space is summarized in Table 6, where T is the wave period in s, and H is the wave height in m at 1:33-scale. Wave generation was found to be highly repeatable for each of the wave cases marked with an x; wave cases that were not found repeatable were not considered. Because it is not possible to measure purely excitation waves at the device location with the FOSWEC device installed and the wave-device interactions will generate additional waves, wave data for the proceeding analysis comes from the wave calibration study for the appropriate wave case.

The wave excitation force is most commonly calculated in the frequency domain, where it is a complex value, having both a magnitude $|F_{exc}(\omega)|$ and a phase $\angle F_{exc}(\omega)$ relative to the amplitude and phase of the wave field. In this way, the wave excitation force can be represented as:

$$F_{exc}(\omega) = f_{exc}(\omega)\eta(\omega) \tag{12}$$

where $f_{exc}(\omega)$ is the complex excitation force/torque coefficient as a function of frequency, and $\eta(\omega)$ is the frequency domain representation of the measured wave surface elevation time series $\eta(t)$.

For analysis of the regular wave excitation, $\eta(t)$ was restricted to 20 crest-to-crest wave cycles for which the first crest was at a minimum of 75% of the maximum recorded wave height for the run. This criteria ensured that the wave field considered was fully developed and excluded initial transients related to start-up of the wave maker. Further, limiting the sampling duration ensures the actual wave field is well approximated by $\eta(t)$ (as determined by the wave calibration study for which the FOSWEC was absent) and that device-generated waves do not have sufficient time to reflect off of basin boundaries and affect the measured forces after propagating back to the device. The measured forces over this time interval were considered. Each time series was low-pass filtered via a first-order back-to-back finite impulse-response filter to remove instrument noise without introducing a phase shift. The amplitudes of the (nominally) sinusoidal time series' were calculated for force and wave height for each cycle, and the median ratio for each cycle was taken as an estimate of the average excitation coefficient magnitude. A 95% confidence interval was calculated by examining the standard deviation of the $f_{exc}(\omega)$ calculated for each of the included 20 cycles.

By using multiple regular wave runs at various amplitudes and periods, an estimate of $f_{exc}(\omega)$ was determined, and its nonlinear dependence on wave amplitude was assessed.

4.4. Forced oscillation

The forced oscillation test objectives are to experimentally determine the added mass, $A(\omega)$, total damping, $C_{tot}(\omega)$, and quadratic drag, C_D. This test was run in still water by controlling the PTO to force the flap to oscillate at different combinations of periods and amplitudes with the platform constrained in all degrees of freedom, and measuring the corresponding force. The radiation damping force refers to the forces exerted on an oscillating body by the wave radiated as a result of the body's oscillation. The radiation force in the time domain is defined by the convolution integral, Eq. (2). Under this operating condition, the dynamic equation for the flap in pitch simplifies to:

$$F_{pto}(t) - K_{hs}\theta = (I_{yy} + A_{55})\ddot{\theta} + C_{tot}\dot{\theta} + C_D|\dot{\theta}|\dot{\theta} \tag{13}$$

where $F_{pto}(t)$ is the driving PTO force, $C_{tot}(\omega) = B_{55}(\omega) + C_v(\omega)$ is the total linear damping at the oscillation frequency consisting of radiation damping, $B_{55}(\omega)$, and the linear viscous damping coefficient, $C_v(\omega)$, and $C_D(\omega)$ is the quadratic drag term.

Pursuant to the DOE Public Access Plan, this document represents the authors' peer-reviewed, accepted manuscript. The published version of the article is available from the relevant publisher.

Table 6
Regular wave cases at 1:33-scale marked with x (3x indicates repeated run).

H (m)	$H_3 = 0.136$		x	x	x	x	x	x
	$H_2 = 0.045$	x	3x	x	3x	x	3x	x
	$H_1 = 0.015$	x	x	x	x	x	x	
		$T_1 = 0.87$	$T_2 = 1.22$	$T_3 = 1.57$	$T_4 = 1.91$	$T_5 = 2.26$	$T_6 = 2.61$	$T_7 = 3.31$
	T (s)							

As shown in Eq. (13), by subtracting the hydrostatic contribution from the measured PTO force, the added mass, $A_{55}(\omega)$, total damping, $C_{tot}(\omega)$, and quadratic drag, $C_D(\omega)$, can be extracted by considering different points in the forced oscillation. Forced sinusoidally, a point of maximum velocity has an acceleration of zero, and vice versa. Ideally, this allows for the damping forces proportional to velocity to be separated from the inertia forces proportional to acceleration by analyzing velocity maxima and acceleration maxima separately, as in Beatty et al. (2015). However, in practice, velocity maxima did not occur simultaneously at zeros of acceleration, and vice versa, likely due to a small 'dead band' observed in the flap position sensor near $x = 0$ and drive-train slack. As such, this method was not perfectly applicable for the FOSWEC data set.

Further, work by Brown et al. (2017) has highlighted the frequency independence of C_D over small ranges of the Keulegan–Carpenter (KC) number, which can be calculated for the prescribed sinusoidal oscillations:

$$KC = \frac{|\dot{\theta}|T}{L} \tag{14}$$

where $|\dot{\theta}|$ is the amplitude of the angular velocity oscillation, T is the period of oscillation, and L is the amplitude of oscillation in rad. Traditionally, KC is derived in terms of linear distances and translational velocities. The KC number was found to be nearly constant across prescribed tested conditions for forced oscillation, and therefore C_D was presumed constant over the range of ω tested. The range of KC numbers is calculated from observed test conditions to validate this assumption. Additionally, simulation results were found to be insensitive to adjustments to C_D within an order of magnitude, so any modeling errors introduced due to this approximation are minor.

The considered time series was restricted to symmetric oscillations at the prescribed amplitude, and filtered using the same method as in the wave excitation studies. This served to exclude any transients related to start-up, and to reduce the impact of any position-varying parameters. For some test cases, this combination of conditions severely limited or entirely eliminated the available data—these cases have been flagged in the data set. Beginning at a velocity peak, the data were then windowed to one half of an oscillation period, ensuring both large accelerations and velocities would be included in the window. Because $\dot{\theta}|\dot{\theta}|$ is highly correlated with $|\dot{\theta}|$ it is not possible to solve simultaneously for C_D and C_V in a least squares sense, so a two-step procedure was adopted. Firstly, hydrostatic contributions were subtracted from each window and Eq. (13) was solved in a least-squares sense for damping and added mass, assuming all damping (drag, viscous, and radiation), C_{lin}, is proportional to pitch velocity:

$$F_{pto} - K_{hs}\theta = \begin{bmatrix}\dot{\theta} & \ddot{\theta}\end{bmatrix}\begin{bmatrix}C_{lin}\\ I_{yy} + A_{55}\end{bmatrix} \tag{15}$$

Then, using different amplitudes of $|\theta|$ at a given frequency, the linearization proposed by Inman (2008) and utilized by van Riij et al. (2017) was adopted to calculate a C_D estimate for each oscillation frequency via linear regression:

$$F_{vis} = C_{lin}\dot{\theta} = (C_{tot} + 8C_D\omega|\theta|/(3\pi))\dot{\theta} \tag{16}$$

such that the y-intercept of the fitted line is the linear damping term C_{tot} (the combination of radiation and viscous damping) and the slope proportional to $8\omega|\theta|/(3\pi)$ is the quadratic coefficient, C_D. By earlier arguments, C_D is assumed to be constant over tested conditions, and as such, the estimates for C_D for each frequency of oscillation were averaged for a more robust estimate.

With the estimate for C_D, the contribution of quadratic drag was removed along with hydrostatic contributions from the measured force and the added mass and linear damping parameters were recalculated for each test case by:

$$F_{pto} - K_{hs}\theta - C_D|\dot{\theta}|\dot{\theta} = \begin{bmatrix}\dot{\theta} & \ddot{\theta}\end{bmatrix}\begin{bmatrix}C_{tot}\\ I_{yy} + A_{55}\end{bmatrix} \tag{17}$$

where $C_{tot}(\omega)$ is the frequency-dependent contribution of the linear damping. Details of the resulting comparisons between experimental data and numerical simulations will be detailed in the following sections.

4.5. Regular wave

The objective of the regular wave test is to characterize the FOSWEC's response to regular waves with various device configurations, corresponding to Config 1– Config 4. In the first configuration, Config 1, only the front flap's motion in pitch is free to move. Config 2 allows both flaps to pitch, and thus includes the motion of two interacting flaps. Config 3 allows both flaps to pitch and the platform to move in heave. The final configuration, Config 4, allows both flaps to pitch, and the platform to move in heave, pitch, and surge. For wave response tests, the wave basin generated several sets of regular wave fields (see Table 6).

Measurement of the FOSWEC motion was achieved via encoders mounted on each flap to measure pitch response, and sensors mounted on the platform to measure response in heave, pitch, and surge, refer to Fig. 1. Additionally, 6-DOF load cells were mounted on each shaft to measure the loads on the flaps, and a 6-DOF load cell was mounted on the arm's connections to the platform to measure its loads.

Results from regular wave response tests are presented as response amplitude operators (RAOs) for each of the four FOSWEC configurations, where the RAO is defined as the ratio between the magnitude of response to the incident wave height:

$$RAO(\omega) = \frac{|X|}{H} \tag{18}$$

where $|X|$ is the peak-to-peak motion response magnitude, and H is the wave height, as determined from a corresponding wave calibration run. For translational motion response, the RAO has units of m/m, and, for rotation motion response, the RAO has units of deg/m. Similar to the data analysis of the wave excitation tests, analysis of the regular wave response X was filtered and restricted to ensure that the wave field considered was fully developed and excluded initial transients related to start-up of the wave basin. RAOs were then calculated using 20 crest-to-crest wave cycles of fully developed response.

5. Results

5.1. Static offset

Static offset tests were performed for the flap in pitch and the platform in heave, pitch, and surge—corresponding to each of the FOSWEC's degrees of freedom. These tests were performed by offsetting the body in each degree of freedom, holding it statically at varying displacements, and measuring the resulting force/torque. For more

Pursuant to the DOE Public Access Plan, this document represents the authors' peer-reviewed, accepted manuscript. The published version of the article is available from the relevant publisher.

Table 7
Hydrostatic stiffness from static offset tests with the correlation coefficient compared to WAMIT solution.

Static offset	K_{hs}	WAMIT	Experimental	R^2
Flap pitch	k_{55} (Nm/deg)	0.63	1.2	0.972
Platform heave	k_{33} (N/m)	5,610	7,150	0.999
Platform pitch	$k_{55,p}$ (Nm/deg)	21.2	39.8	0.996
Platform surge	k_m (N/m)	N/A	963	0.961

information about the hydrostatic test setup, refer to Bosma et al. (2016) and Sandia National Laboratories (2019a).

When running WEC-Sim with linear hydrostatics, the hydrostatic restoring force is modeled as a function of the body's displacement multiplied by a constant hydrostatic stiffness coefficient, K_{hs}, as defined in Eq. (4). When hydrostatic stiffness is modeled as a constant coefficient, a linear regression was fit between measured force/torque and displacement, and the correlation coefficient, R^2, of the fit was calculated. Any nonlinearity will reduce R^2. An overview of the resulting K_{hs} and R^2 values for each DOF is presented in Table 7, and a discussion of the results is given in the following sections. The experimentally derived K_{hs} is always larger than the hydrostatic stiffness determined by the WAMIT solution. This is because, in the as-built system, there are stiffness terms in addition to hydrostatic stiffness, caused by the physics of joints, constraints, PTOs, and the surge-restoring bungees.

5.1.1. Flap pitch

The relationship between hydrostatic torque measured at the hinge and angular displacement of the FOSWEC flap is shown in Fig. 5 (top left). As expected from the flap's geometry, the hydrostatic torque increases with flap angular displacement, because the perpendicular distance to the flap center of mass at which the buoyancy force acts increases with the displacement angle, refer to Eq. (7). In addition, since the flap is a wedge shape which is above the water surface at equilibrium, the relationship between water displacement and flap displacement in pitch is expected to be nonlinear. This results in a slightly higher correlation coefficient for a quadratic fit ($R^2 = 0.988$) when compared to the linear regression. The results of this test demonstrate that while k_{55} may be slightly nonlinear, a linear hydrostatic stiffness for the flap in pitch is still an appropriate assumption. However, the effect of this nonlinearity is most pronounced at small and large angles of displacement, and the resulting linear fit predicts zero force at zero displacement. Inspection of the experimental data (and the polynomial fit) indicates a nonzero torque value at zero displacement, indicating the presence of static friction. Significant static friction is unsurprising, given the large drivetrain gear ratio, and highlights a shortcoming of the linear fit. The experimentally determined hydrostatic stiffness is nearly double the WAMIT estimate. The flap pitch static offset test was performed with the flap PTO connected and there is additional stiffness in the system caused by the physics of the PTO drivetrain not modeled by WAMIT.

5.1.2. Platform heave

The relationship between hydrostatic force measured from the overhead crane and displacement of the FOSWEC platform in heave is shown in Fig. 5 (top right). For translation in heave, the FOSWEC has a strongly linear relationship between measured force and displacement, with a hydrostatic stiffness of $k_{33} = 7150$ (N/m) and correlation coefficient of $R^2 = 0.9998$. A linear relationship for k_{33} is expected in this range because, while there are changes in the cut waterplane area of the platform in heave for very large displacements ($z_{min} = -0.06$ m and $z_{max} = 0.37$ m) when the platform is fully submerged or out of the water, the static offset test was performed for displacements with small changes in the cut waterplane area. The results of this test demonstrate that a linear hydrostatic stiffness for the platform in heave is appropriate. However, comparison of the experimentally derived stiffness to the hydrostatic stiffness determined by WAMIT, $k_{33} = 5610$ N/m, demonstrates that the motion constraint in heave provides an additional stiffness that is not fully captured by hydrostatics alone, as shown in Table 7.

5.1.3. Platform pitch

The relationship between hydrostatic torque and rotation of the FOSWEC platform in pitch is shown in Fig. 5 (bottom left). Similar to the results for heave, for rotation in pitch the FOSWEC also has a strongly linear relationship between measured torque and displacement, with a hydrostatic stiffness of $k_{55,p} = 39.8$ Nm/deg and a correlation coefficient of $R^2 = 0.996$. The strongly linear relationship for $k_{55,p}$ is expected because while there are changes in the submerged volume of the platform in pitch, the FOSWEC platform's pitch range of motion is small (less than 10°), so the resulting change in displaced volume is relatively small. Again, a comparison of the experimentally derived stiffness to the hydrostatic stiffness determined by WAMIT, $k_{55,p} = 21.2$ Nm/deg, indicates nonhydrostatic sources of stiffness (Table 7). Note that in both experimental and WAMIT evaluations, the platform pitch and heave hydrostatic responses are evaluated with the flaps attached, as there were no considered device configurations in which the flaps were not present.

5.1.4. Platform surge

As mentioned in the previous section, there is no hydrostatic restoring force in surge. Bungee cords were installed on the FOSWEC's motion constraint arm in lieu of a traditional mooring system to restore the FOSWEC's displacement in surge; therefore, no restoring force from WAMIT. The surge static offset test was used to characterize the bungee force as a function of surge displacement. The relationship between hydrostatic force measured from the overhead crane used to laterally displace the device and translation of the FOSWEC platform in surge is shown in Fig. 5 (bottom right). Of the static offset tests performed, the surge test had the poorest linear fit between measured force and displacement, with a surge mooring stiffness of $k_m = 963$ N/m and a correlation coefficient of $R^2 = 0.961$ (see Table 7). However, while the other linear fits had higher correlation coefficients, the linear regression for surge force still appears to capture the overall trend of the data. Particularly, the nonzero intercept predicted by the linear fit indicates the presence of significant static friction in the surge guiderails, and deviations from the linear trend suggest nonlinear behavior in the bungees.

5.2. Free decay

Free-decay tests were performed by offsetting the body to various initial displacements in each degree of freedom, releasing the body from its initial displacement, and measuring the resulting motion response to steady-state equilibrium. The purpose of the free decay test was to determine the natural period, T_n, of the FOSWEC in each DOF, and estimate the corresponding total damping, C_{tot}, as described in Table 5. Additionally, the flap free decay test was used to validate estimates of C_{tot} and C_D calculated separately from forced oscillation testing.

An overview of the results from the free decay tests is shown in Table 8, and details of each test will be described in the following sections. Recall that C_D for flap pitch (indicated by an asterisk in Table 8) was calculated from Eq. (11) using an added mass estimate from forced oscillation testing, while other C_D values were selected by tuning parameters. Further, the added mass estimate used to normalize flap pitch damping coefficients was from forced oscillation experimental data, while other degrees of freedom were estimated using BEM added mass predictions.

Pursuant to the DOE Public Access Plan, this document represents the authors' peer-reviewed, accepted manuscript. The published version of the article is available from the relevant publisher.

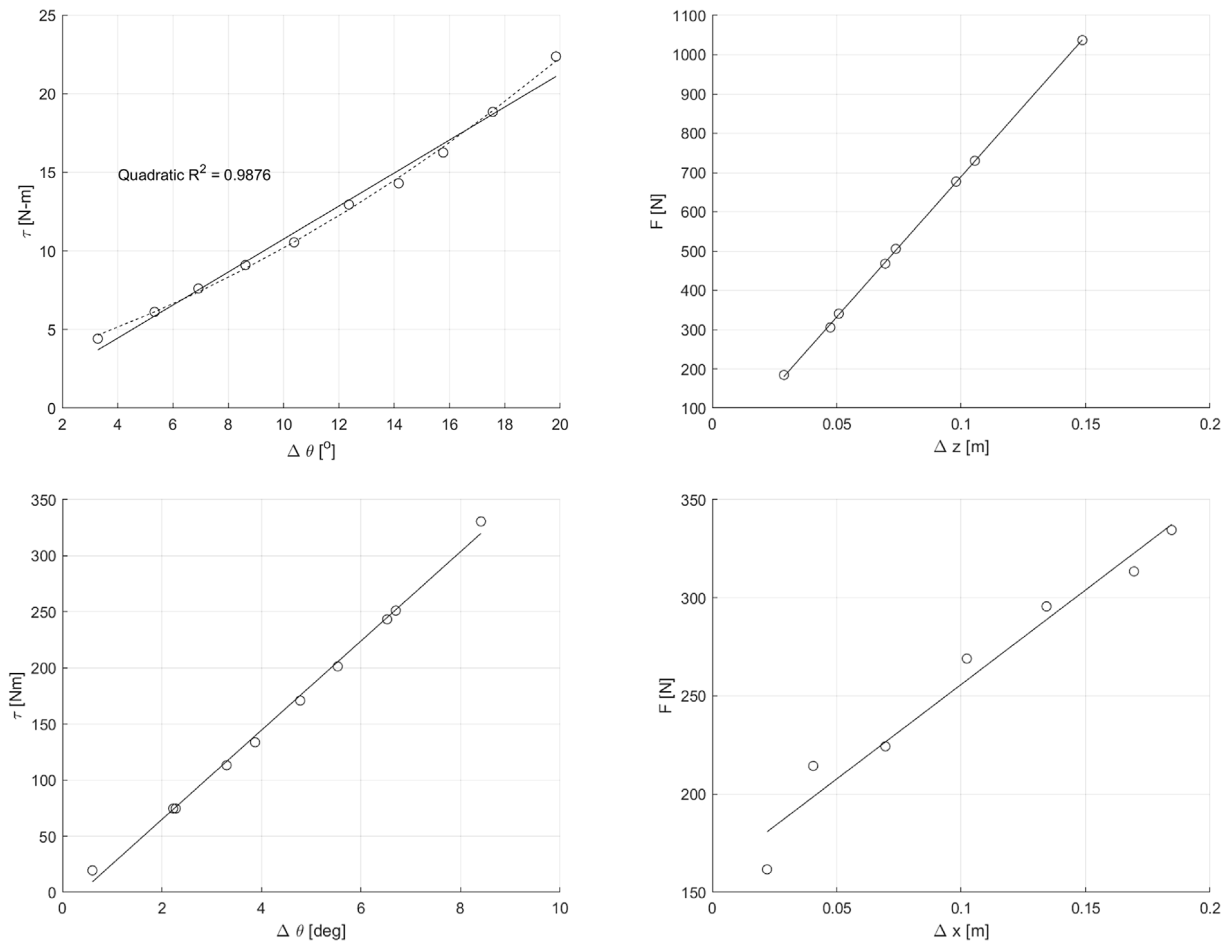

Fig. 5. Measured hydrostatic loads as a function of displacement for flap pitch (top left), platform heave (top right), platform pitch (bottom left), and platform surge (bottom right). Solid lines represent linear fits to the data, and, for the flap, the dashed line illustrates the polynomial fit.

Table 8
Free decay mean damped natural period (experimental and simulation), viscous damping, and drag at the damped natural period for each DOF.

Free Decay	$T_{d,exp}$	$T_{d,sim}$	C_v	C_D
Flap pitch	4.37 s	4.44 s	4.84 (Nms/rad)	7.45* (Nms^2/rad^2)
Platform heave	1.54 s	1.36 s	502.4 (Ns/m)	300 (Ns^2/m^2)
Platform pitch	1.67 s	1.64 s	14 (Nms/rad)	25.2 (Nms^2/rad^2)
Platform surge	N/A	N/A	347 (Ns/m)	7808 (Ns^2/m^2)

5.2.1. Flap pitch

The flap decay for each initial displacement is shown in Fig. 6 (top left) with 95% confidence intervals indicated at the minimums and maximums utilized by the logarithm decrement method. The damping ratio for each initial displacement was calculated, and the mean total damping, C_{tot}, was determined. The total damping was then subtracted by the radiation damping to determine the mean viscous damping, $C_v = 4.68$ Nms/rad, which was applied in the WEC-Sim simulation on the flap in pitch. Similarly, a drag of $C_D = 7.45\,\mathrm{Nm/rad^2/s^s}$, the product of the slope of Eq. (11) and $(I_{yy} + A_{55})$, the added mass estimate from the tested forced oscillation frequency $\omega = 1.90$ rad/s, the closest to ω_d was used in simulation. The comparison between these parameters and those derived from forced oscillation testing is discussed in the forthcoming section.

The experimentally observed natural period is relatively constant for each initial displacement, with a damped natural period of 4.43 s, 4.35 s, and 4.33 s for the 10°, 15°, and 20° initial offsets, respectively. The corresponding simulated flap pitch decay damped natural periods, estimated as the time from release to the first local maximum, are 4.37s, 4.35 s, and 4.32 s. A comparison of the experiment to simulation results shows that WEC-Sim accurately estimates the damped natural period, and that the pitch decay rate accurately approximates the experimental rate until the oscillations become <10% of the initial displacement. It should be noted that although the results of the flap static offset include the PTO drivetrain, the flap free decay tests were performed with the PTO drivetrain disconnected to approximately isolate the hydrodynamic effects. However, the more abrupt decay in experiment suggests that the static bearing friction, not modeled in simulation, likely becomes significant for small flap oscillations.

5.2.2. Platform heave

The platform heave decay results for each initial displacement are shown in Fig. 6 (top right) with 95% confidence intervals indicated at the minimums and maximums. The mean viscous damping was determined to be $C_v = 502.4$ Ns/m, which was then applied in the WEC-Sim simulations for the platform decay in heave. Because forced oscillation tests were not completed for the platform, drag was used as a tuning parameter, and a drag of $C_D = 300$ Ns^2/m^2 was selected to provide the best fit.

As shown in Fig. 6 (top right), the experimental natural period for each heave decay initial displacement remains relatively constant, slightly increasing with larger initial displacement. The experimental heave decay damped natural periods are 1.52 s, 1.54 s, and 1.56 s for the 7 cm, 10 cm, and 15 cm initial offsets, respectively. The corresponding simulated platform heave decay damped natural periods are 1.35 s, 1.36 s, and 1.38 s. While there is a discrepancy between the experimental and simulated natural periods, it can be observed that the

Pursuant to the DOE Public Access Plan, this document represents the authors' peer-reviewed, accepted manuscript. The published version of the article is available from the relevant publisher.

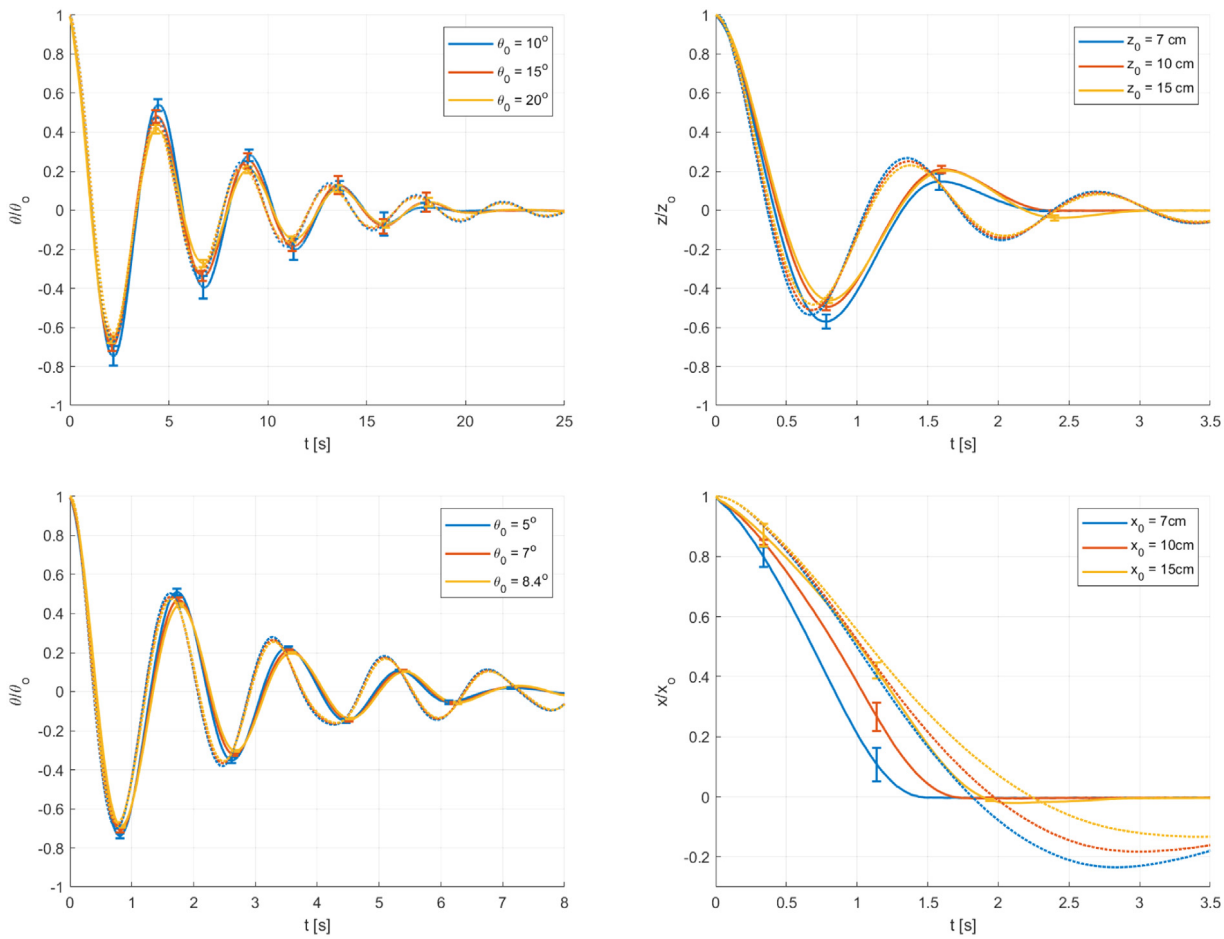

Fig. 6. Free decay tests for flap pitch (top left), platform heave (top right), platform pitch (bottom left), and platform surge (bottom right). Minimums and maximums are shown with 95% confidence intervals. Dotted lines correspond to WEC-Sim simulations. Results have been normalized by initial displacements.

WEC-Sim simulations are within the 95% confidence intervals at the first negative peak ($t = 0.72$s), capturing both the period and magnitude of oscillation. The difference between simulated and observed heave decay occurs at small relative displacements ($z/z_0 < 0.2$) and is likely due to unmodeled static friction in the heave telescoping constraint. This effect is exemplified through the experimental results for the smallest initial displacement of $z_0 = 7$ cm when compared to the larger initial displacements, wherein the first negative peak has the largest relative displacement, but the smallest relative displacement at the first positive peak ($t = 1.51$ s). This experimental observation is typical of a system dominated by friction. An overview of these experimental and simulated results is shown in Table 8.

5.2.3. Platform pitch

The platform pitch decay for each initial displacement is shown as Fig. 6 (bottom left) with 95% confidence intervals indicated at the minimums and maximums. The mean viscous damping, C_v = 14 Nms/rad, was applied in the WEC-Sim simulation on the platform in pitch. Because forced oscillation tests were not completed for the platform, drag was used as a tuning parameter, and a drag of C_D = 25.2 Nm/rad^2/s^s was selected to provide the best fit. The natural period is relatively constant for each initial displacement, with a damped natural period of 1.66 s, 1.68 s, and 1.68 s for the 5°, 7°, and 8.4° initial offsets, respectively. The corresponding simulated platform pitch decay damped natural periods are 1.63 s, 1.64 s, and 1.66 s. Like the flap pitch decay test, the pitch decay rate is slightly overdamped in the experimental data compared to the simulations. This is demonstrated by the fact that the simulation results are within the 95% confidence intervals for the regions of larger relative displacement ($\theta/\theta_0 > 0.3$). This again suggests that unmodeled static friction may become significant at small displacements.

5.2.4. Platform surge

The platform surge decay for each initial displacement is shown as Fig. 6 (bottom right) with 95% confidence intervals indicated. Because this oscillation is an overdamped system, the logarithmic decrement method is inappropriate for damping ratio determination. The damping ratio and natural frequency for each initial displacement was instead calculated using an iterative least-squares fit of the canonical equation of a normalized damped harmonic oscillator:

$$y(t) = 1 - \exp(-\zeta\omega_n t)\cos(\omega_n t\sqrt{1-\zeta^2}) + \zeta\sqrt{(1-\zeta^2)}\sin(\omega_n t\sqrt{1-\zeta^2}) \quad (19)$$

using MATLAB's *fminsearch* function. From the fitted damping ratio and natural frequency, the mean total damping, C_{tot}, was determined using the same method as for previous free decay tests. The total damping was then subtracted by the radiation damping to determine the mean viscous damping, C_v = 347 Ns/m, and was applied in the WEC-Sim simulation on the platform in surge. Because forced oscillation tests were not completed for the platform, drag was used as a tuning parameter, and a drag of C_D = 7808 Ns^2/m^2 was selected to provide the best fit. Based on the results from the static offset test in surge, a mooring stiffness of k_m = 963 N/m was applied in surge to model the effect of the bungees. The surge decay experimental and numerical comparison shows that the results decay at a similar rate, but the WEC-Sim results have substantial overshoot in comparison to the experimental data. This is likely because the bungees are nonlinear

Pursuant to the DOE Public Access Plan, this document represents the authors' peer-reviewed, accepted manuscript. The published version of the article is available from the relevant publisher.

in nature and the presence of unmodeled static friction along the surge guide rail. Nonetheless, the numerical and experimental comparison is acceptable considering the underlying dynamics for surge decay are not modeled by hydrodynamics; the driving force in this case is the restoring bungee force. It should also be noted that the large drag is expected because the surge decay test was performed with both flaps locked in the vertical position, so any movement in surge would have to overcome a large drag force caused by the surface area of the flaps, refer to Eq. (5).

5.3. Wave excitation

The purpose of the wave excitation test is to determine the wave excitation force coefficient, f_{exc}, on flap 1, as described in Table 5. Wave excitation tests were performed by locking the flap motion in pitch, and measuring the resulting wave loading at the load cell mounted on the hinge. This experiment was performed for a range of incident wave conditions, corresponding to the regular waves with different combinations of wave period and wave height, as listed in Table 6. Results from the wave excitation experiments were then compared to the flap's BEM solution in WAMIT, which were calculated with the origin at the hinge location to restrict all wave excitation to the pitch DOF. This allows for direct comparison to the experimental results.

A comparison between wave excitation force coefficients, f_{exc}, for flap 1 measured from regular wave experiments with 95% confidence intervals, and the corresponding BEM solution from WAMIT is shown in Fig. 7. The experimentally determined wave excitation force coefficient was measured from the load cell mounted on the flap's shaft, thus the relevant DOF is flap rotation in pitch. Because WEC-Sim solves for a WEC's motion about each body's c_g, the BEM solution used by WEC-Sim must be solved at the c_g. However, for these comparisons, the WAMIT solution was solved with the origin at the hinge location to allow for direct comparison between the measured wave excitation force coefficient from the experiments to that from WAMIT. Analysis of the experimentally determined wave excitation from regular wave tests does not show a strong dependence on wave height. This is demonstrated by the fact that over most of the explored wave frequencies, the measured wave excitation force coefficients fall within the 95% confidence intervals of the other wave heights. This confirms the linear assumption for wave excitation on the flap, meaning that the wave excitation coefficient for the flap can be assumed to be frequency-dependent, but not also amplitude-dependent. It should be noted that at $\omega = 4$ rad/s, the largest wave height exhibited overtopping, reducing the excitation force coefficient significantly over the smaller wave heights.

Fig. 7 shows that the measured wave excitation force coefficients follow a similar curve shape as the WAMIT solution; however, WAMIT consistently underpredicts the excitation force coefficient for wave frequencies $\omega \leq 4$ rad/s, corresponding to $T \geq 1.57$ s. The underprediction of the wave excitation coefficient from the WAMIT solution for $T \geq 1.57$s is expected because WAMIT only solves for the excitation force on the wetted surface of the body in still water. However, substantial wave runup and overtopping were observed during the wave excitation tests, especially for the longer wave periods. The runup and overtopping were partially caused by the fact that the FOSWEC platform was fixed in order to measure the wave excitation force, thus the FOSWEC was unable to heave along with the free surface, as would typically be the case for floating bodies. Additionally, the FOSWEC flaps are surface piercing with a freeboard of 0.12 m, and wave excitation tests were performed for wave heights of $H = 0.015$ m, 0.045 m, and 0.136 m. As a result, the experimentally derived wave excitation coefficient is expected to have a larger magnitude because the true wetted surface of the flap and resulting torque are larger than those solved for by WAMIT.

A notable departure from the experimental trend occurs for $\omega = 5.2$ rad/s, for which experimental estimates of wave excitation exhibit substantially increased uncertainty (i.e. large standard deviations) and reduced mean values. Both flaps were locked vertically during the excitation tests. This resulted in standing waves, reflections from downstream flap contained by the buoyancy floats. At this frequency, these reflections were significant and out of phase with the upstream flap, as evidenced by an atypically large excitation coefficient for flap 2 at this frequency (not shown). This interference decreased the observed load on flap 1 and reduced the excitation coefficient. Further, the phase variation between the excited wave and the radiated wave from the second flap would contribute to the higher cycle-to-cycle variation observed in the excitation coefficient. Since this WAMIT was run using only a single flap (excluding the downstream flap and buoyancy floats), this body-to-body interaction was not present in BEM parameter estimates. The BEM estimate would have likely been more representative if the downstream flap was locked in a horizontal position such that wave reflections were reduced.

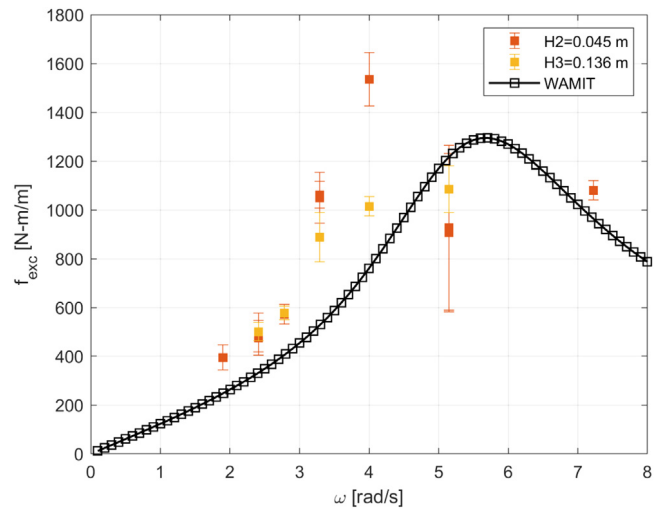

Fig. 7. Comparison between experimentally determined wave excitation coefficient and the WAMIT solution for flap rotation in pitch about the hinge.

Table 9
Summary of Keulegan–Carpenter numbers observed during forced oscillation testing.

Min	Mean	Max	Std. Dev
0.465	0.850	1.330	0.250

5.4. Forced oscillation

The purpose of the forced oscillation tests was to determine the added mass, $A_{55}(\omega)$, and radiation damping, $B_{55}(\omega)$, components of the radiation force on flap 1, as described in Table 5. Forced oscillation tests were performed in still water by controlling the PTO to force flap 1 to oscillate at different combinations of periods and amplitudes. The force required to drive the flap in oscillation was measured, corresponding to the radiation force. By subtracting the hydrostatic and quadratic damping contributions to measured force according to Eq. (13), an experimental estimation of viscous damping and added mass were made, assuming a constant C_D over the relatively constant KC number. The observed KC numbers calculated using Eq. (14) show small variation, as shown in Table 9.

At high frequencies of forced oscillation, particularly at high amplitudes, wave overtopping was prevalent. As a result, Eq. (16) does not have a positive slope at these frequencies, yielding a nonphysical negative estimate for C_D. Further, asymmetric oscillations were more prevalent under high-frequency test conditions, decreasing the number of valid tests and, as a result, the number of points in the linear regression Eq. (16), diminishing confidence in this estimate.

Pursuant to the DOE Public Access Plan, this document represents the authors' peer-reviewed, accepted manuscript. The published version of the article is available from the relevant publisher.

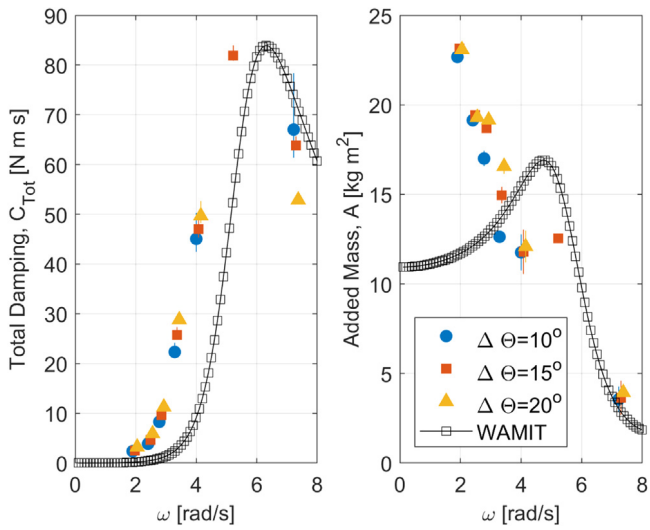

Fig. 8. Forced oscillation tests and the BEM solution from WAMIT: (left) estimates of linear damping and (right) added mass.

Finally, Brown et al. (2017) derives the KC number independence of C_D using Morison's equation, which is appropriate for slender bodies for which wave diffraction effects can be neglected. At higher tested frequencies this is a poor assumption for the FOSWEC device because the wavelength implied at these frequencies approximates flap length. For these reasons, estimations of C_D were excluded from the average for cases $\omega > 5$ rad/s. This resulted in a C_D estimate of 14.22 Nm/rad^2/s^2.

Comparisons of the experimentally determined added mass, $A_{55}(\omega)$, and radiation damping, $B_{55}(\omega)$, to the BEM solution from WAMIT are shown in Fig. 8. In Fig. 8, experimentally determined $C_{tot}(\omega)$ and $A_{55}(\omega)$ are plotted with colored squares for each oscillation amplitude, and results from the BEM solution in WAMIT are plotted with a solid black line. Bars indicate the 95% confidence interval of least-squares parameter estimation for each calculation window. Small bars indicate little cycle-to-cycle variation.

As expected, the experimentally determined total damping, $C_{tot}(\omega)$, is much larger than the WAMIT solution of $B_{55}(\omega)$, shown on the left-hand side of Fig. 8. This is unsurprising, as the BEM solution is based on a potential-flow solution method, and thus excludes the contribution due to viscosity, $C_v(\omega)$. In order to determine the contribution due to viscosity, $C_v(\omega)$, was applied in all WEC-Sim simulations, and the difference between $C_{tot}(\omega)$ and $B_{55}(\omega)$ was used. Similarly, a comparison between the experimentally determined added mass and the WAMIT solution is shown on the right-hand side of Fig. 8. BEM added mass underpredicts experimental results at low frequencies, corresponding to $\omega < 3$ rad/s, and overpredicts for $3 < \omega < 6$ rad/s. Note that the resulting estimate of C_{tot} at the highest frequency is less than the BEM-estimated damping, implying $C_v < 0$, refer to Eq. (17).

In addition to the comparison of the WAMIT solution to the experiments it is worth noting the effect of oscillation amplitude on experimentally determined coefficients. Each of the forced oscillation tests was performed for the range of oscillation periods defined in Table 6, and for three different magnitudes corresponding to $\Delta\theta = 5°$, 10°, and 20°, where $\Delta\theta$ is the difference between the maximum displacement and steady-state equilibrium. The experimentally determined $C_{tot}(\omega)$ only demonstrates significant dependence on oscillation magnitude for the largest wave frequency, where a larger oscillation magnitude corresponds to smaller total damping. At midrange frequencies ($\omega \sim 4$ rad/s, $\omega \sim 3$ rad/s), there is a smaller dependence on magnitude, and the trend is reversed: larger oscillations exhibit increased damping. The experimentally determined $A_{55}(\omega)$ only demonstrates amplitude dependence for $\omega = 3.3$ rad/s, where the numerical result agrees closely with the experimental results.

Using the $\omega = 1.9$ rad/s forced oscillation case, the average of the added mass values (as there is little amplitude dependence) was multiplied with the free-decay mass-normalized estimates of damping coefficients, refer to Eq. (11) and Table 8, for comparison with forced oscillation-derived damping estimates. The discrepancy between forced oscillation and free-decay damping estimates is small, unlikely to affect simulation accuracy, and is explainable.

First, the trend in added mass suggests that the added mass at ω_d likely was larger than at $\omega = 1.9$ rad/s; therefore, the decay-test damping estimates were likely underestimated by this method. Second, C_D can only be presumed constant for a constant KC number. While that was shown to be approximately true for forced oscillation testing, it is untrue for free-decay tests, which oscillate at a fixed period T_d, but through diminishing velocity amplitude. A free-decay test would have covered a range of KC numbers, and some discrepancy in C_D estimate might thus be expected. Meanwhile, the C_v estimate from free decay appears to be smaller than the forced oscillation estimate, perhaps again suggesting an underestimated added mass. The experimentally derived $C_v(\omega)$ and C_D terms from forced-oscillation testing were applied to all regular wave simulations based on their observed frequency and amplitude dependence.

5.5. Wave response

The purpose of the wave response test was to characterize the FOSWEC's response to regular waves with various device configurations, corresponding to Config 1–Config 4, as described in Table 5. Wave response tests were performed for four different configurations of the FOSWEC, each with different degrees of freedom and resulting dynamics. Config 1 corresponds to flap 1 pitch motion, Config 2 corresponds to flap 1 and flap 2 pitch motion, Config 3 corresponds to the addition of platform heave motion, and Config 4 allows both flaps to pitch and the platform to move in heave, pitch, and surge. The Directional Wave Basin at the Hinsdale Wave Research Laboratory generated regular wave fields, which is summarized in Table 6 at 1:33-scale. These wave cases were selected because they were found to be highly repeatable during the wave calibration runs. Each of the wave cases listed in Table 6 were run once for Config 1, and all of the wave cases except $H_1 = 0.015$ m were run for Config 2–Config 4. To simplify comparisons between configurations, H_1 results are omitted from Config 1 plots. For all configurations wave cases of $H_2 = 0.045$ m and $T = 1.22$, 1.91 and 2.61 s were repeated three times to demonstrate the repeatability of the measured RAO response. In the following sections, comparison of the experimentally measured response of the FOSWEC is compared to the numerical simulations for the same conditions. The results are presented as RAOs for each of the four FOSWEC configurations, where the RAO is defined by Eq. (18).

5.5.1. Config 1

Comparison of the experimentally determined RAO for Config 1 to WEC-Sim simulations is shown in Fig. 9. Experimentally measured RAOs are plotted with colored squares for each wave height, and RAO results from WEC-Sim simulations are plotted with dotted lines and square markers. Standard deviation bars refer to the standard deviation of the parameter estimation for each cycle. Small standard deviation bars indicate little cycle-to-cycle variation.

For the WEC-Sim RAOs, the simulations were run with linear hydrodynamics, which explains why the resulting simulations have similar trends for different wave heights. WEC-Sim closely estimates the RAO for all wave frequencies except the lowest frequency. This is expected because the flap is near resonance at the lowest wave frequency, and potential flow-based codes are known to be inaccurate near resonance. This is exemplified through the comparison between the experimentally derived radiation terms shown in Fig. 8. For all of the WEC-Sim simulations, the radiation damping and drag coefficients were modified based on the results of the forced oscillation tests in the form of C_v

Pursuant to the DOE Public Access Plan, this document represents the authors' peer-reviewed, accepted manuscript. The published version of the article is available from the relevant publisher.

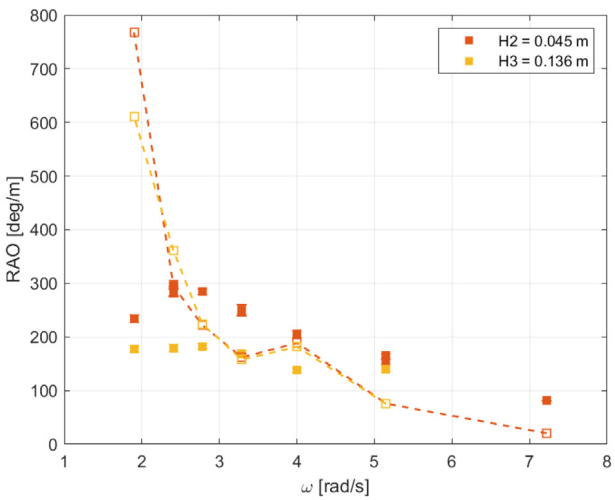

Fig. 9. Config 1 RAO for flap 1. Experimental results denoted by filled squares with error bars, simulations denoted by squares with dashed line.

and C_D; however, the added mass was not adjusted. The experimentally determined added mass $A_{55}(\omega)$ is much larger than the BEM solution for $\omega < 3$ rad/s, which explains why the WEC-Sim simulation overpredicts the flap's pitch motion response for low frequencies. Additionally, the presence of static friction (as suggested during hydrostatic and decay tests) would likely reduce the experimentally observed RAO magnitude for cases of lower wave excitation forces, which inspection of Fig. 7 suggests will occur at the lowest tested wave frequency. If the simulation had been adjusted to account for the experimentally derived added mass, and modeled the static friction, the simulated RAO near the resonance would likely have better agreement with the measurements. This is an area of future investigation. Nonetheless, the simulated RAO has good agreement with the experimental values for most wave periods.

5.5.2. Config 2

Comparison of the experimentally determined RAOs for Config 2 to WEC-Sim simulations are shown in Fig. 10. Similar to the results from Config 1, WEC-Sim does a good job estimating the RAOs for both flaps at all wave frequencies except the lowest frequency. The explanation for this discrepancy is also similar, since for Config 2 each of the flaps' added mass at low frequencies was significantly underestimated by the WAMIT solution. However, for wave frequencies greater than the flap's resonance $\omega > 2$ rad/s, the RAO response is within reasonable error.

5.5.3. Config 3

Comparison of the experimentally determined RAOs for Config 3 to WEC-Sim simulations are shown in Fig. 11. Similar to Config 1 and Config 2, WEC-Sim simulations for Config 3 were run with linear hydrodynamics. The simulated and experimental RAO response for flaps 1 and 2 are similar to those from Config 2, and demonstrate the same divergence near resonance and agreement for $\omega > 2.5$rad/s. Config 3 is the first configuration to include the motion response from the platform, where the platform is free to move in heave.

Unlike the characterization of the flap through forced oscillation tests, the platform did not undergo tests to experimentally determine $C_{tot}(\omega)$, $C_D(\omega)$, and $A(\omega)$. As a result, the hydrodynamic coefficients for the platform are based on the results from the WAMIT solution, C_v from free decay testing, and C_D used as a tuning parameter. Nonetheless, the numerical simulations from WEC-Sim for the platform's heave motion response agree well versus the experimental RAOs at all wave frequencies. The WEC-Sim results systemically overpredict the platform's heave response, but they are within reasonable error and predict the overall shape of the RAO curve well. WEC-Sim overprediction of the heave response is likely because the physics of motion constraint are not fully captured in the simulation, particularly any influence of static friction, the presence of which was suggested by the hydrostatic and free-decay tests for this degree of freedom. As discussed in previous sections, the motion constraint provided a mechanism through which the FOSWEC could be easily configured to operate in different degrees of freedom.

5.5.4. Config 4

Comparison of the experimentally determined RAOs for Config 4 to WEC-Sim simulations are shown in Fig. 12. The simulated and experimental RAO response for flap 1, flap 2, and platform heave are similar to those from Config 3, albeit with a notable reduction in experimental platform heave RAO amplitude for $\omega >= 3.29$ rad/s, indicating that the availability of surge and platform pitch degrees of freedom reduces heave response at these frequencies. In addition platform heave and both pitching flaps, Config 4 also includes platform motion in surge and pitch. As with platform heave, forced oscillation tests were not performed on the platform, hydrodynamic coefficients for the platform were determined in the same way as Config 3. Additionally, for the surge DOF, a mooring stiffness, k_m, was applied based on the surge static offset test. Particularly at low frequencies, experimental surge RAO magnitudes show a strong dependence on wave height, while the simulated RAO shows significantly less sensitivity. This could be explained by the influence of unmodeled static friction: small waves could not overcome this force, resulting in an RAO near-zero, while large waves could. Significantly larger surge RAOs were observed in the experiment than predicted by simulation, suggesting BEM estimates of hydrodynamic parameters may be poor at these frequencies. For platform motion in pitch, the WEC-Sim RAO estimates the RAO curve shape, but the pitch RAO magnitude is systematically overpredicted for all but the largest wave frequencies. Particularly, simulation predicts a peak at $\omega = 5.2$ rad/s that is not observed in the experimental data.

It is also worth observing the difference in RAOs for the different experimental configurations due to coupling between degrees of freedom. For ease of direct comparison, the RAO for each DOF is plotted on the same axis scale for Config 1–Config 4. Looking at the experimental RAOs for flap 1 across all configurations, it is clear that the experimental RAOs for Config 1 have the largest overall magnitude, with $RAO > 200$ deg/m for $\omega < 4$rad/s for H_2. In this configuration, only flap 1 is allowed to move, thus there is no coupling between degrees of freedom. Once flap 2 is free to move in Config 2, the range of $RAO > 200$ deg/m for flap 1 is reduced for $\omega = 2.8$ rad/s and $\omega = 3.3$ rad/s, corresponding to $T = 2.26$ s and $T = 1.91$ s respectively. Similarly, the inclusion of the platform motion in heave for Config3 reduces the instances of flap 1 $RAO > 200$ deg/m to a single wave frequency, $\omega = 3.3$ rad/s, corresponding to $T = 1.91$ s. And once the platform is free it move in heave, pitch, and surge, there are zero instances of flap 1 $RAO > 200$ deg/m. Similar observations can be made about the effects coupling between degrees of freedom have on other RAOs. Further, it is notable that the observed experimental reduction in RAO of flap 1 is not always reflected by the simulated estimate. This suggests a potential limit of the linear simulation, as, for reasons highlighted above, this reduction is due principally to nonlinear effects. Gaining a better understanding of the influence of coupling between degrees of freedom and body-to-body interactions was the primary motivation for selecting a device like the FOSWEC, which can be configured to include different operating dynamics.

5.6. Time series comparison

In addition to comparing RAOs, it is desirable that a simulation can accurately predict time-resolved WEC behavior when provided with experimentally or numerical estimates of hydrodynamic parameters. To this end, the time series representations of two Config 1 RAOs are presented as Fig. 13. The results provided are for a common wave

Pursuant to the DOE Public Access Plan, this document represents the authors' peer-reviewed, accepted manuscript. The published version of the article is available from the relevant publisher.

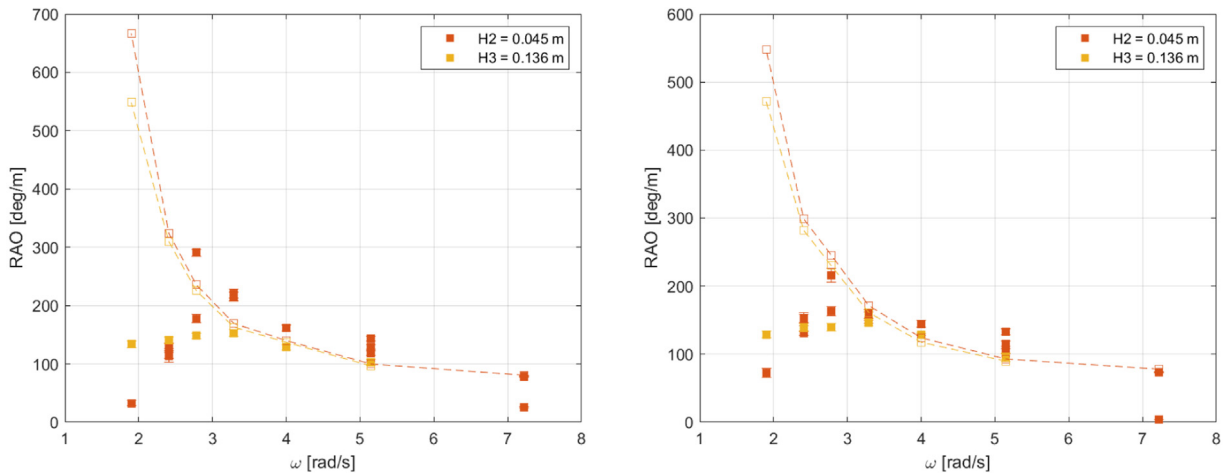

Fig. 10. Config 2 RAO for (left) flap 1 and (right) flap 2. Experimental results denoted by filled squares with error bars, simulations denoted by squares with dashed line.

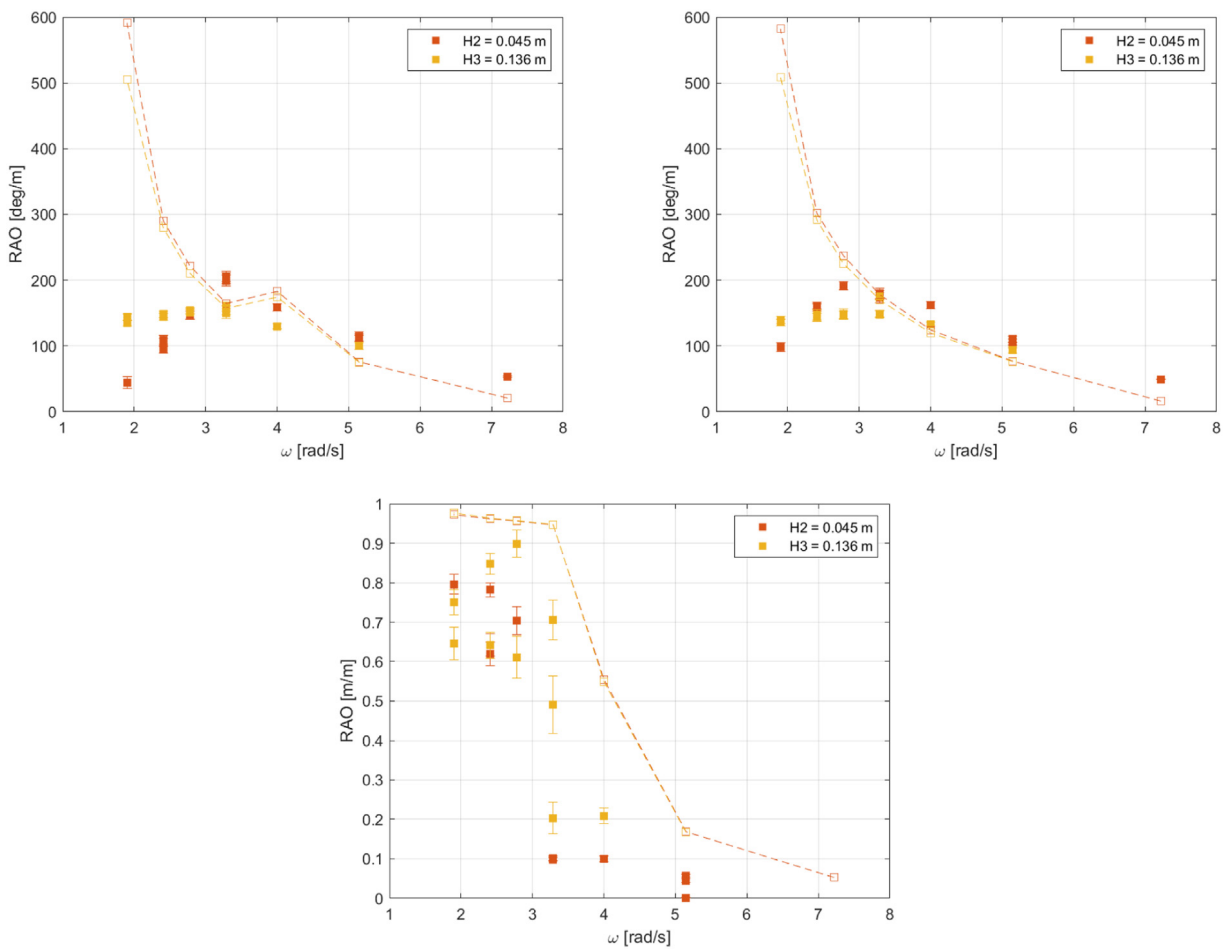

Fig. 11. Config 3 RAO for (top left) flap 1, (top right) flap 2, and (bottom) platform in heave. Experimental results denoted by filled squares with error bars, simulations denoted by squares with dashed line.

period of $T_6 = 2.61$ (s), but for two different wave heights, $H_2 = 0.045$ m and $H_3 = 0.136$ m.

As noted in the previous discussions, the error in the $H_3 = 0.136$ m case is attributed to nonlinear (position-dependent) response to wave excitation. Larger waves tended to oscillate the flaps more asymmetrically in the experiment. As mean flap angle departs from zero, only a component of the wave excitation force will impart flap motion, resulting (generally) in simulation overpredicting the RAO for larger wave heights. The relative asymmetry of the experimental data and the reduced amplitude of oscillation align with this reasoning.

For the common frequency of oscillation, it is unlikely that unmodeled static friction drives error in the second case. The larger error occurs for the larger $H_3 = 0.136$ m wave, for which there would be larger forces than the well-modeled $H_2 = 0.045$ m wave case, further reducing the impact of static friction (which already appears to be negligible for the smaller wave case). This suggests that the asymmetric

Pursuant to the DOE Public Access Plan, this document represents the authors' peer-reviewed, accepted manuscript. The published version of the article is available from the relevant publisher.

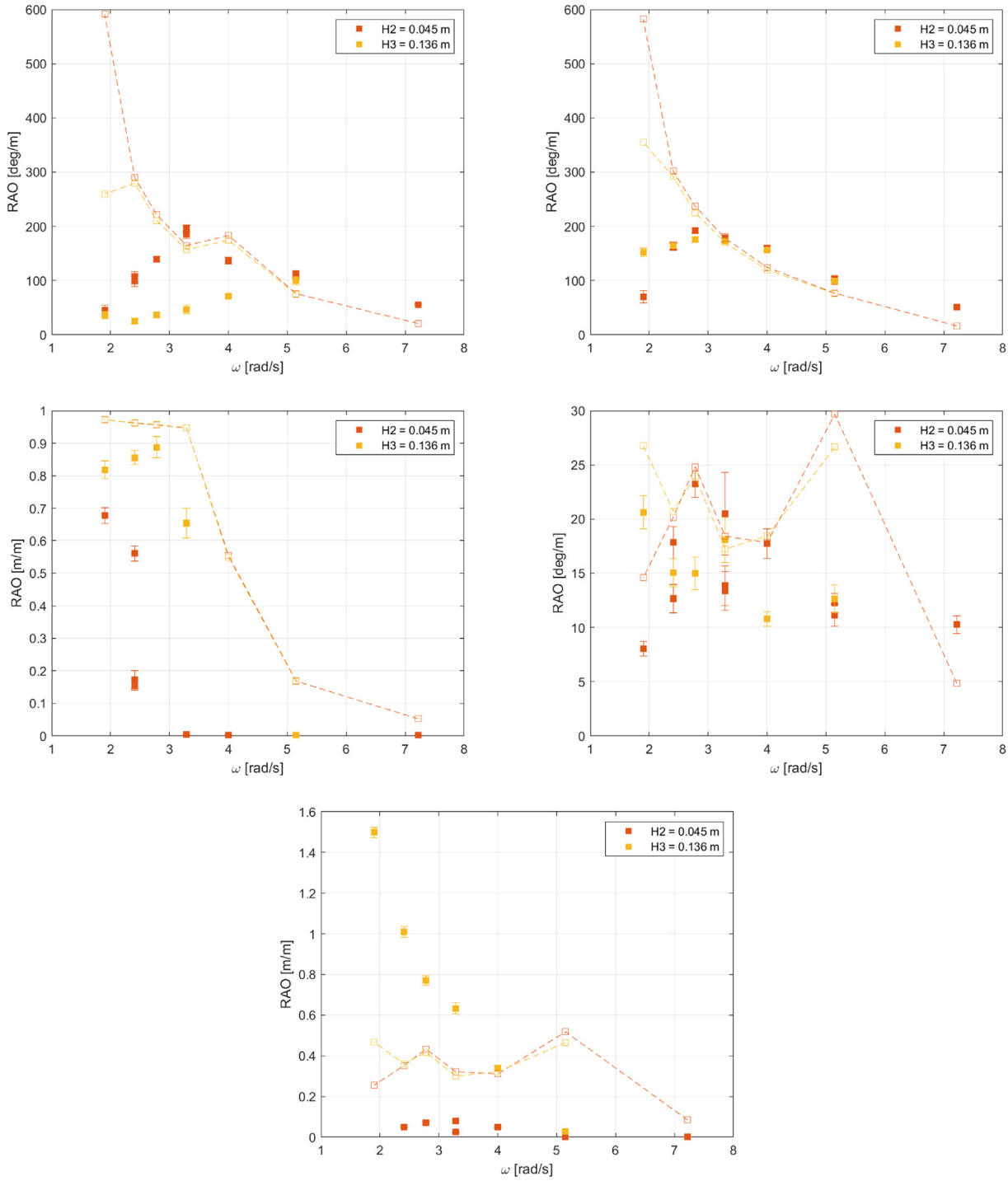

Fig. 12. Config 4 RAO for (top left) flap 1, (top right) flap2, and (middle left) platform in heave, (middle right) pitch, and (bottom) surge. Experimental results denoted by filled squares with error bars, simulations denoted by squares with dashed line.

flap oscillation may increase simulation error for high amplitude oscillations, while unmodeled static friction increases simulation error for lower amplitude, lower force operating conditions for which friction dominates.

6. Conclusion

In this study, experimental wave tank tests and numerical simulations of a 1:33-scale floating oscillating surge wave energy converter (FOSWEC) are compared in regular waves. In order to develop an open-access validation data set, the FOSWEC was designed, built, and tested. The device was tested for a range of different conditions including: static offset, free decay, forced oscillation, wave excitation, and response to regular waves. Furthermore, the FOSWEC was tested in four different device configurations (Config 1–Config 4). The details of the experimental setup and data analysis for each of the FOSWEC tests are described in this paper, and the experimental data, simulations, and processing for the FOSWEC are available on public repositories in an open-access format. Data from the experimental test were then compared to numerical simulations using the open-source WEC-Sim code, informed by the BEM solution, calculated using WAMIT. The WAMIT solution was evaluated *a priori* (i.e., unadvised by experimental

Pursuant to the DOE Public Access Plan, this document represents the authors' peer-reviewed, accepted manuscript. The published version of the article is available from the relevant publisher.

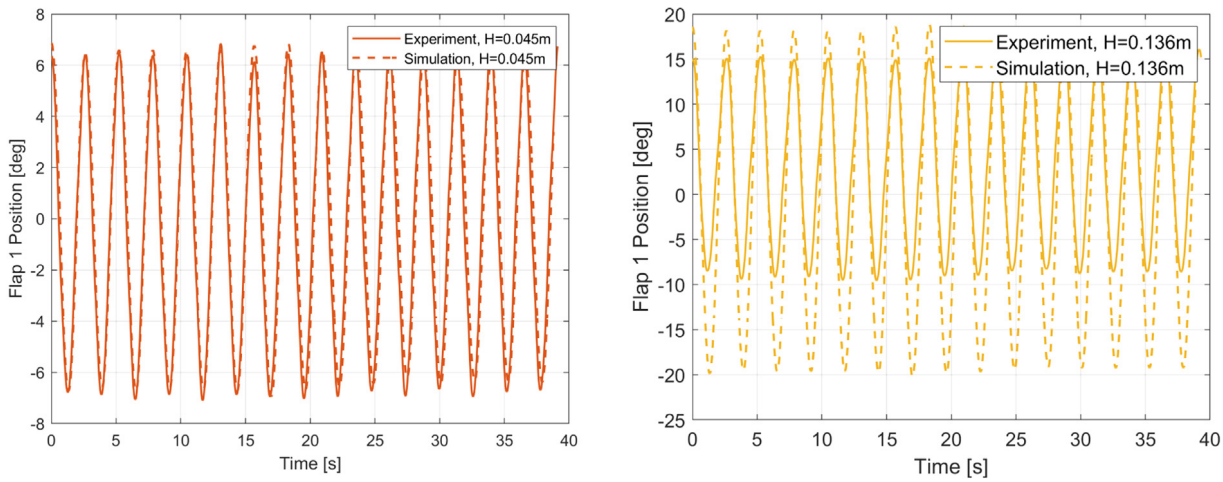

Fig. 13. Time series comparison of simulated and experimental Config 1 RAO tests for $T_6 = 2.61$ s and $H_2 = 0.045$ m (left) and $H_3 = 0.136$ m (right).

data), and the WEC-Sim results were evaluated *a posteriori*, wherein the simulations were tuned based on experimental findings. This comparison between numerical simulations and experiments uses RAOs in each of the degrees of freedom (DOF) to compare the simulated and observed motion response. The results detailed in this paper demonstrate that, with some limitations, WEC-Sim is able to accurately simulate the response of the FOSWEC in each of the four different configurations when subject to regular waves. Based on the limitations determined through this study, the following future work items have been identified.

As exemplified through the comparison of the BEM solution from WAMIT to the experimentally derived coefficients for the flap, a large discrepancy between low-frequency added mass estimates contributed to systematic overprediction of flap pitch response at these frequencies. The authors of this paper believe that the inclusion of additional added mass for the flap at low wave frequencies would reduce the pitch RAOs substantially and bring the simulations into agreement with experiments. However, the WEC-Sim code does not currently allow users to directly import experimentally derived coefficients such as added mass, particularly when these parameters are derived in a distinct coordinate system from that used in simulation. Users are able to augment existing BEM radiation damping and added mass data, but there is no way to directly import frequency- and amplitude-dependent experimentally derived coefficients. Notably, while much attention in the literature has been given to determination of viscous damping and drag, these results suggest that equal attention should be paid to improving the accuracy of added mass estimates. Further, the discrepancy between BEM and experimentally derived estimates for the flap suggest that similar differences are likely for the platform, highlighting the potential importance of forced oscillation testing in each degree of freedom for which accurate added mass estimates are essential to useful simulation results.

Substantial modeling errors were observed for degrees of freedom subjected to small excitation loads and displacements due to the presence of unmodeled static friction. While modeling accuracy could be enhanced through the inclusion of a static friction model, it is noted that static friction is undesirable in a power-producing WEC and accurate modeling for low excitation conditions is of less interest than accuracy near power-producing conditions (where static friction is, ideally, insignificant). A static friction model is therefore a lower-priority improvement than allowing for direct definition of experimentally determined added mass. In addition to work identified as a result of the regular wave simulation and data analysis, future work beyond the scope of this publication includes expanding the numerical and experimental FOSWEC comparison to irregular waves and loads characterization. Incorporating nonlinear hydrodynamics, including Froude–Krylov forces, to the WEC-Sim simulation will provide an additional point of comparison, potentially improve simulation performance, and further specify sources of discrepancy between experiment and simulation.

Acknowledgments

The authors would like to thank the following people for their support of WEC-Sim validation testing and data analysis: Pedro Lomonaco, Bret Bosma, Ratanak So, and Asher Simmons from Oregon State University's O.H. Hinsdale Wave Research Laboratory, Andrews–Cooper for the design and fabrication of the FOSWEC, +D for design and fabrication of the motion constraint, and Budi Gunawan, Giorgio Bacelli, Christopher A. Kelley, Chris Simmons, and Carlos Michelen from Sandia National Laboratories. Funding provided by the U.S. Department of Energy, Office of Energy Efficiency and Renewable Energy, United States of America, Water Power Technologies Office, United States of America. Sandia National Laboratories is a multimission laboratory managed and operated by National Technology and Engineering Solutions of Sandia, LLC., a wholly owned subsidiary of Honeywell International, Inc., for the U.S. Department of Energy's National Nuclear Security Administration under contract DE-NA0003525. This work was also authored by the National Renewable Energy Laboratory, operated by the Alliance for Sustainable Energy, LLC, for the U.S. Department of Energy under Contract No. DE-AC36-08GO28308. The views expressed in the article do not necessarily represent the views of the DOE or the U.S. Government.

References

Beatty, S.J., Hall, M., Buckham, B.J., Wild, P., Bocking, B., 2015. Experimental and numerical comparisons of self-reacting point absorber wave energy converters in regular waves. Ocean Eng. 104, 370–386. http://dx.doi.org/10.1016/j.oceaneng.2015.05.027.

Bosma, B., Ruehl, K., Simmons, A., Gunawan, B., Lomonaco, P., Kelley, C., 2016. WEC-Sim phase 1 validation testing - Experimental setup and initial results. In: Proceedings of the ASME 2016 35th International Conference on Ocean, Offshore and Arctic Engineering.

Brown, A., Thomson, J., Rusch, C., 2017. Hydrodynamic coefficients of heave plates, with application to wave energy conversion. IEEE J. Ocean. Eng. PP, 1–14. http://dx.doi.org/10.1109/JOE.2017.2762258.

Combourieu, A., Lawson, M., Babarit, A., Ruehl, K., Roy, A., Costello, R., Weywada, P.L., Bailey, H., 2015. WEC 3: Wave energy converter code comparison project. In: Proceedings of the 11th European Wave and Tidal Conference.

Cruz, J., 2008. Ocean Wave Energy: Current Status and Future Prespectives. Springer.

Cummins, W.E., 1962. The Impulse response function and ship motions 9 (47) (1962) 101–109. http://dx.doi.org/1962.

Folley, M., 2016. Numerical Modelling of Wave Energy Converters: State-of-the-Art Techniques for Single Devices and Arrays. Academic Press.

Pursuant to the DOE Public Access Plan, this document represents the authors' peer-reviewed, accepted manuscript. The published version of the article is available from the relevant publisher.

Garcia-Rosa, P.B., Costello, R., Dias, F., Ringwood, J.V., 2015. Hydrodynamic modelling competition: Overview and approaches. In: Proceedings of the ASME 34th International Conference on Ocean, Offshore and Arctic Engineering.

Hinsdale, O.H., Wave Research Laboratory, Oregon State University, URL http://wave.oregonstate.edu/.

Inman, D., 2008. Engineering Vibration. Pearson Education, Inc., pp. 43–48.

Josset, C., Babarit, A., Clement, A., 2007. A wave-to-wire model of the SEAREV wave energy converter. J. Eng. Marit. Environ. 221 (2), 81–93. http://dx.doi.org/10.1243/14750902JEME48.

Lawson, M., Garzon, B.B., Wendt, F., Yu, Y.-H., Michelen, C., 2015. COER hydrodynamics modeling competition: modeling the dynamic response of a floating body using the WEC-Sim and FAST simulation tools. In: Proceedings of the ASME 34th International Conference on Ocean, Offshore and Arctic Engineering.

Lee, C.-H., Newman, J.N., 2017. Wamit. URL http://www.wamit.com/.

Lopez, I., Andreu, J., Ceballos, S., Martínez de Alegría, I., Kortabarria, I., 2013. Review of wave energy technologies and the necessary power-equipment. 27, 413–434. http://dx.doi.org/10.1016/j.rser.2013.07.009.

MHKDR, 2019. Marine and Hydrokinetic Data Repository, URL https://mhkdr.openei.org/.

OPERA, 2019. Open Sea Operating Experience to Reduce Wave Energy Cost (OPERA), URL http://opera-h2020.eu/.

van Riij, J., Yu, Y.-H., Edwards, K., Mekhiche, M., 2017. Ocean power technology design optimization. Int. J. Mar. Energy 20, 97–108. http://dx.doi.org/10.1016/j.ijome.2017.07.010.

Ruehl, K., Michelen, C., Bosma, B., Yu, Y.-H., 2016. WEC-Sim phase 1 validation testing - Numerical modeling of experiments. In: Proceedings of the ASME 2016 35th International Conference on Ocean, Offshore and Arctic Engineering.

Ruehl, K., Michelen, C., Kanner, S., Lawson, M., Yu, Y.-H., 2014. Preliminary verification and validation of WEC-Sim, an open-source wave energy converter design tool. In: Proceedings of the ASME 2014 33rd International Conference on Ocean, Offshore and Arctic Engineering.

Sandia National Laboratories, 2019. Experimental Testing of a Floating Oscillating Surge Wave Energy Converter at Hinsdale Wave Research Laboratory, URL https://mhkdr.openei.org/submissions/310, https://dx.doi.org/10.15473/1508364.

Sandia National Laboratories, 2019. FOSWEC data processing scripts, URL https://github.com/WEC-Sim/FOSWEC.

Weber, J., 2012. WEC technology readiness and performance matrix - finding the best research technology development trajectory. In: Proceedings of 4th International Conference on Ocean Energy.

WEC-Sim, 2019. WEC-Sim (Wave Energy Converter SIMulator) code, URL https://github.com/WEC-Sim/WEC-Sim.

Wendt, F., et al., 2017. International energy agency ocean energy systems task 10 wave energy converter modeling verification and validation. In: Proceedings of the 12th European Wave and Tidal Conference.

Pursuant to the DOE Public Access Plan, this document represents the authors' peer-reviewed, accepted manuscript. The published version of the article is available from the relevant publisher.